A Fundamental Mechanism of Solar Eruption Initiation

Chaowei Jiang,[1*] Xueshang Feng,[1*] Rui Liu,[2,3] XiaoLi Yan,[4]
Qiang Hu,[5,6] Ronald L. Moore,[5] Aiying Duan,[7]
Jun Cui,[7] Pingbing Zuo,[1] Yi Wang,[1] Fengsi Wei[1]

[1]Institute of Space Science and Applied Technology,
Harbin Institute of Technology, Shenzhen 518055, China
[2]CAS Key Laboratory of Geospace Environment,
Department of Geophysics and Planetary Sciences,
University of Science and Technology of China, Hefei 230026, China
[3]CAS Center for Excellence in Comparative Planetology, Hefei 230026, China
[4]Yunnan Observatories, Chinese Academy of Sciences, Kunming 650216, China
[5]Center for Space Plasma and Aeronomic Research,
The University of Alabama in Huntsville, Huntsville, AL 35899, USA
[6]Department of Space Science, The University of Alabama in Huntsville, Huntsville, AL 35899, USA
[7]School of Atmospheric Sciences, Sun Yat-sen University, Zhuhai 519000, China

*To whom correspondence should be addressed;
E-mail: chaowei@hit.edu.cn, fengx@spaceweather.ac.cn.

January 13, 2022

Abstract

Solar eruptions are spectacular magnetic explosions in the Sun's corona and how they are initiated remains unclear. Prevailing theories often rely on special magnetic topologies which, however, may not generally exist in the pre-eruption source region of corona. Here using fully three-dimensional magnetohydrodynamic simulations with high accuracy, we show that solar eruption can be initiated in a single bipolar configuration

with no additional special topology. Through photospheric shearing motion alone, an electric current sheet forms in the highly sheared core field of the magnetic arcade during its quasi-static evolution. Once magnetic reconnection sets in, the whole arcade is expelled impulsively, forming a fast-expanding twisted flux rope with a highly turbulent reconnecting region underneath. The simplicity and efficacy of this scenario argue strongly for its fundamental importance in the initiation of solar eruptions.

1 Introduction

From time to time, the Sun produces eruptive activities, such as solar flares and coronal mass ejections (CMEs). It is now confirmed that such eruptions are explosive releases of magnetic energy in the Sun's corona [1]. Research on solar eruptions has a long history of more than a century, from which a basic physical picture has been established [2, 3]. Prior to eruptions, the coronal magnetic field is line-tied at the solar surface (i.e., the photosphere), and is continuously but rather slowly stressed by motions at the photosphere (such as surface shear and rotational flows) that could last for a few hours or even days, during which magnetic free energy accumulates. Since plasma is strongly-magnetized in the corona, the Lorentz force dominates and is mostly self-balanced, that is, the outward magnetic pressure of the low-lying, strongly stressed flux is cancelled by the inward magnetic tension of the overlying, mostly un-sheared flux. At a critical point, there is a catastrophic disruption of this force balance, and the free magnetic energy is rapidly converted into impulsive heating and fast acceleration of the plasma. If the overlying flux is not too strong, the eruptive magnetic field can successfully eject into the heliosphere, forming a CME. Otherwise, it fails to escape, resulting in a confined flare or failed eruption.

A fundamental question that still lies in this picture, also a central point of controversy, is how the pre-eruption force balance is abruptly destroyed. Due to the lack of regular measurements of magnetic field in the corona, the mechanism governing the initiation of solar eruptions has remained a subject of intense investigation for decades [3, 4, 5, 6, 7, 8]. The existing theories fall into two categories; one is based on ideal magnetohydrodynamic (MHD) instability and the other on a resistive process, i.e., magnetic reconnection. The first category requires the pre-existence of a magnetic flux rope (MFR), a group of twisted magnetic field lines winding tightly enough about a common axis, in the corona before eruption, for the triggering of eruption to be a loss of equilibrium [9] or ideal instabilities of the MFR, such as torus instability [10, 11, 12, 13, 14]. On the other hand, the most prevailing model based on magnetic reconnection, namely, the breakout model [15, 16, 17, 18], relies on a multipolar magnetic configuration in which there must be a magnetic null point above the sheared magnetic flux, such that reconnection at the null can remove the overlying restraining flux to trigger an eruption.

However, the key prerequisite of magnetic topology for these models, either an

MFR or a null point, may not generally exist in the source region of eruptions, in particular, in solar active regions (ARs). For the MFR-based models, although there is little doubt that MFR constitutes the core structure of CMEs, the existence of MFR before CME initiation is still in intense debates [19]. Almost all the observed features that have been invoked to support the preexistence of MFRs, such as coronal sigmoids and filaments, can also fit in simply sheared arcades with only weak twist [20, 5]. Furthermore, significant magnetic twist is rarely seen before but only observed during filament eruptions [21, 22]. For the breakout model, the coronal null point, which exists primarily in multipolar magnetic configuration, is not universally present in ARs, considering that the commonly-seen ARs are a bipolar configuration consisting of a pair of sunspots with opposite polarities. Furthermore, in this large, multipolar magnetic field, the null point must be situated right above the sheared arcade concentrated around the polarity inversion line (PIL) such that the breakout reconnection can be effective enough, which is difficult to fulfill in reality [23].

Here, with an ultra high-resolution, fully three-dimensional (3D) MHD simulation, we show that solar eruptions can be initiated from a more universal bipolar magnetic configuration without the aforementioned special topology. The simulation covers the whole process from the energy accumulation in the source region to the triggering of eruption and its subsequent evolution. It shows that with surface shear along the PIL of a bipolar field, a vertical current sheet (CS) can spontaneously form above the PIL, essentially between the strongly-sheared legs of the core of the magnetic arcade. Once the CS is sufficiently thin such that ideal MHD is broken down, reconnection sets in and triggers the eruption. The magnetic topology does not change before the eruption, but transforms to a complex one having a highly twisted erupting MFR after the eruption onset. Although such scenario appears to be similar to an early proposed idea, namely the runaway tether-cutting reconnection model [24, 25, 26] which was originally surmised from observation, that model has never been accomplished in 3D simulations and thus remains a conjectural "cartoon". Moreover, our simulation shows that the reconnection not only cuts the magnetic tethers, but also results in strong upward tension force, and it is the latter that plays the key role in driving the eruption.

2 Results

Our simulation solves the full MHD equations with both coronal plasma pressure and solar gravity included. It is started with a potential, bipolar magnetic field that mimics a typical solar AR consisting of a pair of sunspots with opposite magnetic polarities (Fig. 1). In particular, the flux distribution has a relatively strong-gradient and elongated PIL, which is a characteristic magnetic field pattern for eruption-productive ARs [27, 28]. The initial background atmosphere is set in hydrostatic state and configured to simulate typical coronal environment with low plasma β (i.e., ratio of gas pressure to magnetic pressure) and high Aflvén speed (Extended Data

Fig. 1). Then we energize the MHD system by applying anti-clockwise rotational flow to both polarities at the bottom surface. Such a flow follows the contours of the magnetic flux and concentrates near the PIL, thus it preserves the magnetic flux distribution and produces strong shear along the PIL. The flow speed, a few kilometers per second, is smaller than the sound speed by two orders and the Alfvén speed by three orders of magnitude, respectively, thus representing a quasi-static stress of the coronal magnetic field.

Figure 1 and Supplementary Video 1 show evolution of magnetic field lines and electric current structure driven by the rotational flow. Since the surface velocity has the largest gradient across the PIL, it creates strongly-sheared, low-lying magnetic field lines there, and the overall structure resembles an inverse S shape. In details, these highly sheared field lines consist of two groups of J shape having an oppositely curved elbow on their ends, and their arms are sheared past each other above the middle of the PIL, where the electric current is the strongest. Initially the current is volumetric but later it is squeezed into a vertical, narrow layer extending above the PIL as an inverse S shape (Fig. 1C and D), which is reminiscent of hot sigmoid structures often observed prior to flare in the corona. On the other hand, field lines connecting the central parts of the magnetic polarities (analogous to sunspot's umbra) are only weakly sheared, which play the role of the strapping field overlying the inner strongly-sheared core. Clearly, the whole magnetic configuration inflates during the energizing phase as magnetic pressure of the sheared arcade increases continuously, which then stretches outward its overlying field, making the bipolar arcade tend to approach an open field configuration. But the magnetic field is still close to force-free, i.e., the outward magnetic pressure gradient is balanced by the inward magnetic tension force, and furthermore, the strapping field is close to current-free, although it has been greatly strengthened compared with the initial potential field (Extended Data Fig. 2).

The surface flow continuously injects magnetic energy into the simulation volume (Fig. 2A). In the early phase, the magnetic energy increases almost linearly, while the kinetic energy is negligible. Thus almost all the energy brought by the surface flow through Poynting flux is stored in the magnetic field. From around $t = 150$ min to 220 min, the kinetic energy shows a slow rise (Fig. 2A and B), indicating that a small amount of magnetic energy is converted into kinetic energy and gravitational potential energy of the plasma as it expands with the magnetic field. But the system is still quasi static as the kinetic energy remains to be three orders of magnitude less than the magnetic energy, and the velocity in the core of the AR is less than the local Alfvén speed by two orders of magnitude (Fig. 2C).

A sharp transition of the evolution pattern, namely an eruption, occurs at $t = 221$ min as the kinetic energy increases impulsively by nearly two orders of magnitude in about 10 min, amounting to $\sim 5\%$ of the original magnetic energy. Meanwhile, the magnetic energy drops immediately, despite the continual injection of Poynting flux through the bottom surface, indicating that the magnetic energy releases quickly during the eruption. The transition time, i.e., the onset time of eruption, is more distinctly shown by time profiles of the magnetic energy releasing

rate (which is the substraction of the magnetic energy changing rate from the total Poynting flux) and the kinetic energy increasing rate. Both of them increase sharply at the eruption onset, and reach their peaks simultaneously at around $t = 227$ min. The kinetic energy gained by plasma (mainly the CME) accounts for approximately one third of the amount of released magnetic energy, indicating that the flare energy should consume the other two thirds. This is consistent with the energy partition between flare and CME in typical eruptive flares [29]. Also such a synchronization of the evolutions of flare energy releasing rate and CME acceleration agrees well with observations [30]. The impulsiveness of the eruption is further seen from the evolution of velocity at a fixed point in the AR core (Fig. 2C), which increases by more than 10 times in 2 min, reaching an Alfvénic speed of ~ 1000 km s^{-1}. We further trace the rising apex of a single field line (corresponding to a coronal loop in observation) initially in the AR core (Fig. 2D). Prior to the eruption, the loop rises slowly with velocity of ~ 10 km s^{-1}, and once the eruption is triggered, it ascends exponentially, gaining a speed of ~ 700 km s^{-1} in about 5 min before its reconnection with others during the eruption. Such a transition from slow-rise to fast-acceleration phases is frequently observed for ejecting hot coronal loops and filaments in eruptions [31, 32].

The key to understanding how the eruption is triggered lies in the evolution of the central current layer. From Figure 1D to 3A, the current layer is seen to become progressively thinner, essentially in its core where the current density is the largest. The thinning of the current layer occurs in a quasi-static way as driven by the slow shearing motion applied at the bottom surface (Methods A.5). Eventually, the current layer turns into a CS as it thins down to the grid resolution, and fast magnetic reconnection kicks in (Fig. 3 shows result for resolution of 90 km in the main run; see also results of other runs with higher resolutions in Methods A.4 and Supplementary Video 2). This occurs at 221 min, exactly the onset time of eruption shown in the energy evolution. The profile of magnetic field component B_z crossing the CS shows that it thins down to a tangential discontinuity in numerical sense (Fig. 3C), since its thickness is only $2 \sim 3$ grid spacings (e.g., 0.20 Mm) which approaches the limit resolvable by the numerical code. Meanwhile, the current density increases fast in the CS but decreases elsewhere to nearly zero, rendering its profile crossing the CS to a Dirac Delta function. This happens when the field, if with ever increasing magnetic shear in the absence of resistivity, asymptotically reaches a fully open state [33, 34], in which the magnetic energy attains its upper limit (i.e., the Aly-Sturrock limit, which is approximately 1.7×10^{30} erg in our case, see Fig. 2A) and all the field is current-free except in the CS where the current density is infinite (Extended Data Fig. 3). However, such open field can never be reached with finite resistivity, and reconnection is unavoidable once the CS is sufficiently thin. The reconnection starts with the Petschek type [35] as its onset is clearly indicated by bidirectional, collimated Alfvénic outflows from the reconnection site (Fig. 3D). At the onset of the reconnection (or eruption), the vertical length of the CS is about 10 Mm, while horizontally it extends up to over 40 Mm (Fig. 3E), and thus its aspect ratios in the vertical and horizontal directions are estimated to be ~ 40 and 150,

respectively. The reconnection quickly reaches a fast rate of ~ 0.05 as measured by the inflow Alfvénic Mach number, and depends weakly on the Lundquist number (Methods A.7).

Once the reconnection begins, the fast rise of the kinetic energy, i.e., the eruption, ensues, and the subsequent development of the CS is extremely dynamical. At large scale, it exhibits a picture of the standard flare model: a plasmoid originates from the tip of the CS and rises quickly, leaving behind a cusp structure separating post-flare loops from un-reconnected fields (Fig. 4A and Supplementary Video 3). The plasmoid, when initially formed (see Fig. 3B, note that before $t = 221$ min 12 s, the magnetic field exhibits still an arcade configuration, and at $t = 221$ min 54 s a plasmoid is seen at the tip of the CS as a result of reconnection), is very small with size of a few megameters, and expands substantially to hundreds of megameters at the end of the simulation. In 3D, it corresponds to a fast growing MFR (Fig. 5 and Supplementary Video 4), which has a weakly twisted core but wrapped by highly twisted envelope. Meanwhile, an arc-shaped fast magnetosonic shock forms ahead of the plasmoid and later encloses the whole erupting structure. All these evolving structures demonstrate a typical coronal magnetic eruption leading to a CME, as seen in observations (Supplementary Video 5) as well as previous numerical simulations with different scenarios [36, 37, 38]. With the magnetic reconnection proceeds continuously, the cusp structure expands in both vertical and horizontal directions (Extended Data Fig. 4). The apex of the cusp ascends with speed of about 22 km s^{-1}. The transverse expansion of the bottom of cusp, which corresponds to the separation of flare ribbons in observation, goes with a speed of 11 km s^{-1}, while the leading edge of the CME reaches a speed of ~ 600 km s^{-1}. All these apparent motions are quantitatively comparable to observed values in typical eruptive flares [39, 40, 41].

At the onset time of the eruption, the Lundquist number of the CS is on the order of $10^{4\sim5}$ (Methods A.6), and thus fast tearing mode (or plasmoid) instability [42, 43] immediately occurs with the eruption, which fragments the CS and results in strongly turbulent fluctuations in the reconnection (Fig. 4). Such small-scale dynamics emerge only in sufficiently high-resolution computation, and the complexity of the turbulent reconnecting CS increases in even higher resolutions (Methods A.4). In the later phase of the eruption, the CS becomes highly fragmented, and many filamentary currents, which are small plasmoids in two-dimensional (2D) slice and mini flux ropes [44, 45] in 3D (Extended Data Fig. 5), are seen in the lower part of the CS (Fig. 5 and Supplementary Video 6). The turbulent reconnection is manifested as intermittency in the temporal profile of kinetic energy increasing rate (Fig. 2B) and the distribution and evolution of velocity (Fig. 4B).

The eruption is powered by magnetic energy and particularly, here the driver of the eruption comes mainly from the magnetic tension force of the newly reconnected field through its slingshot effect (Methods A.10). As can be seen in Figure 4C, which shows the vertical component of the Lorentz force divided by density (i.e., the vertical acceleration of the plasma), the strongest upward acceleration is always located in the outflow of the reconnection site, whereas near the central part of the

MFR is mostly downward acceleration. Consequently, as the reconnected field lines are incorporated in the MFR, they first experience an impulsive acceleration driven by the strong tension force, and then slow down quickly in the MFR (Supplementary Video 7). The vertical velocity is the strongest in the outflow of the reconnection site (Fig. 4B), and through this high-speed jet flow, the newly reconnected magnetic field lines continually join and pile up in the MFR. Thus our analysis suggests that the on-the-fly formed MFR does not drive the eruption, but is passively pushed by the reconnection outflow, at least before the CME acceleration reaches its peak (i.e., $t = 227$ min). Furthermore, at the onset of eruption, the apex of newly formed MFR is located much lower than the critical height of torus instability (Extended Data Fig. 2), i.e., the height at which the decay index of the strapping field reaches the canonical threshold of 1.5 [10]. Thus, the role of torus instability is minor at the onset of the eruption.

3 Discussion

We have presented a fully 3D MHD simulation of solar eruption produced in a single bipolar magnetic field, encompassing the entire process from the gradual accumulation of magnetic free energy to its sudden release. The simulated initiation process of eruption bears the major characteristic features of eruptive flares that are associated with CMEs, such as the formation of coronal sigmoid, the transition from slow rise to fast acceleration of coronal loop, the elongation and separation motions of double flare ribbons (Methods A.9), the growth of a flaring cusp structure, as well as the escape and expansion of a plasmoid, which evolves into a coherent MFR driving a shock ahead.

Early simulations in 2D or translationally-invariant geometries [46, 47] show that by continuous shearing of its footpoints a magnetic arcade asymptotically approaches an open state containing a CS, which is consistent with the Aly-Sturrock conjecture. However, when one takes into account finite resistivity, the system experiences a global disruption with reconnection setting in at the CS, which, in particular, begins at the point with the largest current density in the CS. Our simulation demonstrated this scenario in fully 3D. That is, prior to eruption, the CS forms internally within the strongly-sheared arcade core in a quasi-static evolution as driven by photospheric shearing motion. It seamlessly transforms to a flare CS once reconnection kicks in and the eruption ensues. As the pre-flare short field lines reconnect to long ones with a double-arc shape, they are concave upward, thus having strong upward tension forces which propel upward the newly reconnected flux from the top of the CS. As a result, more fluxes are allowed to collapse into the CS and then reconnect, which establishes a positive feedback between the escape of the newly reconnected flux and the reconnection. Such a runaway process, as demonstrated being able to be triggered within a sheared, single bipolar field, agrees with the tether-cutting reconnection model [26] (which although conjectures that eruption is driven by the unleashed magnetic pressure). As the reconnection

proceeds from the strongly sheared core flux to the weakly sheared (and nearly current-free) enveloping field, a large-scale MFR is generated as the core of CME with weakly twisted axis wrapped by highly winding field lines. Further mediated by the tearing mode instability, the reconnection runs into a turbulent way, which strongly fragments the CS.

Compared with other fully 3D simulations [36, 48, 13] which also start from a bipolar region that is energized by photospheric flows, ours is unique in twofold. First, we have shown that the eruption can be initiated by shearing solely without flux cancellation. Second, it is unnecessary for an MFR to form before and subsequently trigger the eruption. More importantly, the fact that the central CS forms in a quasi-static way distinguishes ours from other 3D simulations of eruption, in which the CS accounting for flare reconnection forms in a dynamic evolution. For instance, in the MFR-based models, the CS forms after the rise of the unstable MFR, which forces the oppositely-directed field lines below the MFR to approach quickly. Similarly in the breakout model, the central flare CS forms only after a feedback is triggered between the expansion of the inner sheared arcade and the breakout reconnection at the null, in which the central CS is thinned by the fast converging flow induced by the dynamic expansion of the sheared arcade [49]. In contrast, the thinning of CS in our simulation is directly driven by the slow quasi-static shearing, which requires a sufficiently low numerical diffusion in the computation and a high accuracy in the line-tied bottom boundary condition, therefore more challenging than thinning the CS through dynamic inflows (Methods A.5).

In summary, our simulation with sufficiently high fidelity demonstrates a fundamental mechanism for solar eruptions triggered and driven by magnetic reconnection, within the simplest magnetic configuration. Whether the mechanism also applies to cases with photospheric flux cancellation as observed mainly in the decaying phase of ARs [50], or, where a flux rope is built up quasi-statically by much slower reconnection at the photosphere [51] and erupts as it grows to an ideally unstable state [36, 48, 13], will be examined with comparable high-accuracy simulations.

Correspondence and requests for materials should be addressed to C.W.J. and X.S.F.

Acknowledgments. C.W.J. acknowledges support from National Natural Science Foundation of China (NSFC) grants 41822404 and 41731067, the Fundamental Research Funds for the Central Universities (Grant No. HIT.BRETIV.201901), and Shenzhen Technology Project JCYJ20190806142609035. X.S.F. is supported by NSFC grants 42030204, 41861164026 and 41874202 and the Strategic Priority Program of the Chinese Academy of Sciences, Grant No. XDB41000000. R.L. is supported by NSFC grants 41774150 and 11925302 and the Strategic Priority Program of the Chinese Academy of Sciences, Grant No. XDB41030100. X.L.Y. is supported by NSFC grant 11873087, Yunnan Science Foundation for Distinguished

Young Scholars under No. 202001AV070004, and the Yunnan Key Science Foundation of China under No. 2018FA001. Data from observations are courtesy of NASA SDO and STEREO. The computational work was carried out on TianHe-1(A), National Supercomputer Center in Tianjin, China.

Author contributions. C.W.J. conceived the study, developed the numerical MHD model, performed the result analysis and wrote the text. X.S.F. contributed to the design of numerical MHD schemes. R.L., X.L.Y., Q.H., R.L.M., and A.Y.D. contributed to the result analysis. All authors participated in discussions and revisions on the manuscript.

Competing financial interests. The authors declare no competing financial interests.

Data availability. The data generated by the high-resolution 3D MHD simulations and analyzed for this paper occupy a large amount of approximately 10 TB. Interested parties are invited to contact the corresponding authors to make arrangements for the transfer of those data.

Code availability. We have opted not to make our numerical code of the MHD simulation publicly available owing to its complexity, which demands expert assistance to set up, run and analyze simulations, and because it is continually being improved and extended, which requires frequent software updates. Interested parties are invited to contact the authors for more detailed information.

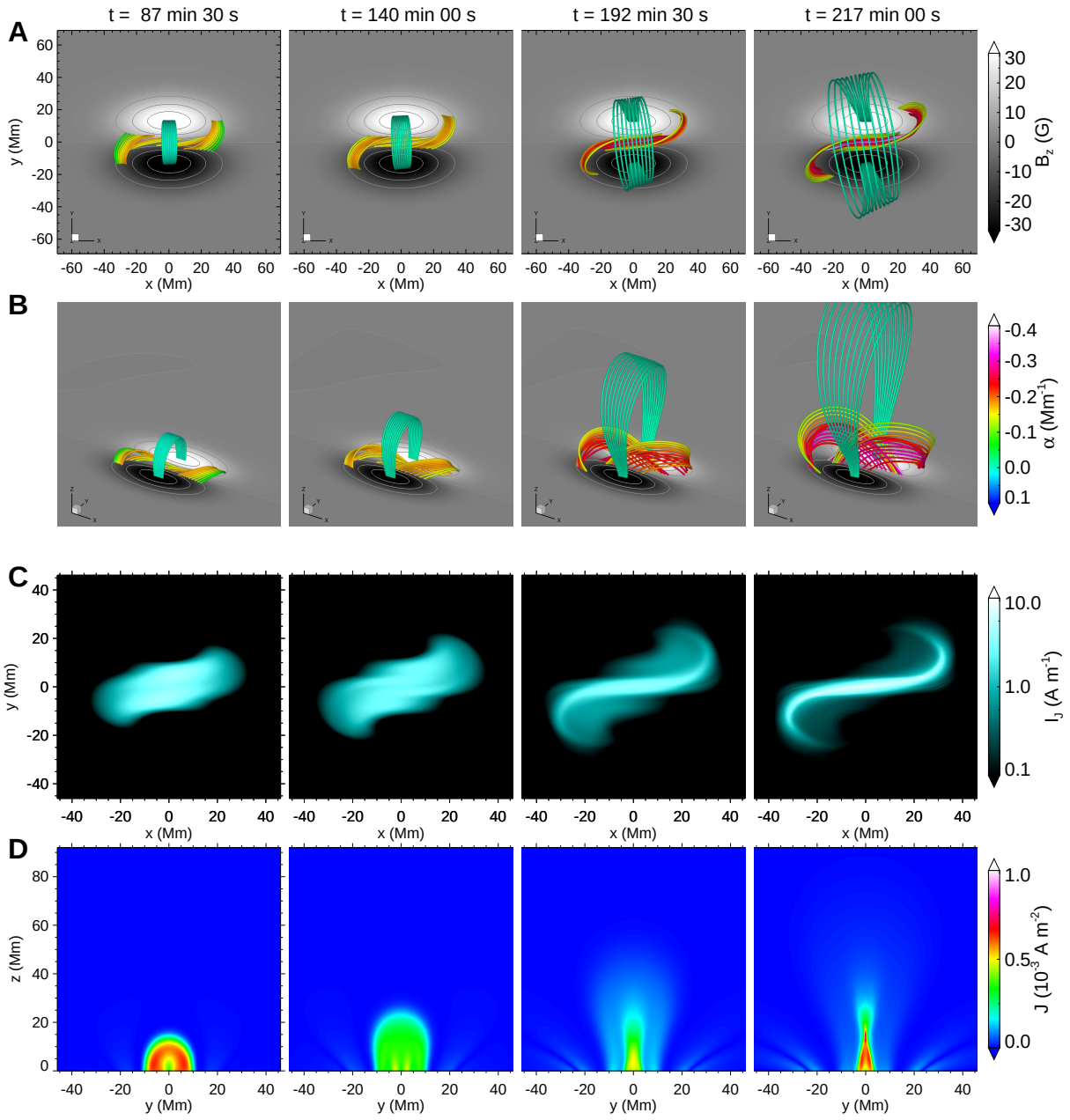

Figure 1: **Evolution of magnetic field lines and electric currents prior to eruption**. **(A)** Top view of magnetic field lines. The colored thick lines represent magnetic field lines and the colors denote the value of nonlinear force-free factor defined as $\alpha = \mathbf{J}\cdot\mathbf{B}/B^2$, which indicates how much the field lines are non-potential. In particular, for a perfectly force-free field, this parameter is constant along any given field line. As can be seen, the magnetic field is close to force-free since the color is nearly the same along any single field line. Note that at all different times, the field lines are traced from the same set of seeds at the bottom surface convected with the surface flow. The background shows the magnetic flux distribution on the bottom boundary (i.e., plane of $z = 0$), and contours of $B_z = (-30, -20, -10, 0, 10, 20, 30)$ G are shown. **(B)** 3D prospective view of the same field lines shown in panel **(A)**. **(C)** Vertical integration of current density, i.e., $I_J = \int J dz$. **(D)** Vertical cross section (i.e., the $x = 0$ slice) of current density.

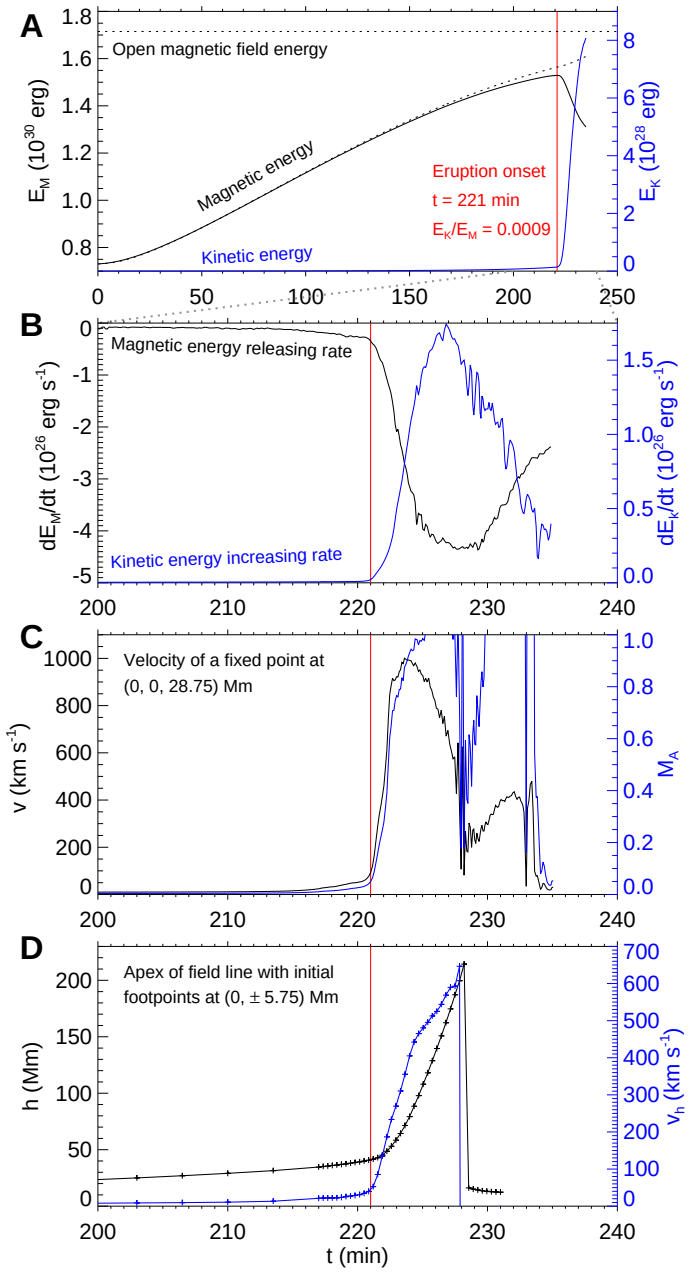

Figure 2: **Temporal evolution of different parameters in the simulations. (A)** Evolution of magnetic energy E_M (the black line) and kinetic energy E_K (the blue line). The dashed curve shows the energy injected into the volume (i.e., time integration of total Poynting flux) from the bottom boundary through the surface flow. The horizontal dashed line denotes the value of the total magnetic energy for a open force-free field with the same magnetic flux distribution on the bottom surface. **(B)** Releasing rate of magnetic energy (the black line) and increasing rate of kinetic energy (the blue line). **(C)** Magnitude of velocity (the black line) and Aflvénic Mach number (the blue line) at a fixed point with location of $(x, y, z) = (0, 0, 28.75)$ Mm. **(D)** Height (the black line) and rising speed (the blue line) of the apex of a magnetic field line in the AR's core initially overlying the current sheet. In all panels, the red lines are shown for denoting the transition time (at $t = 221$ min) from pre-eruption to eruption.

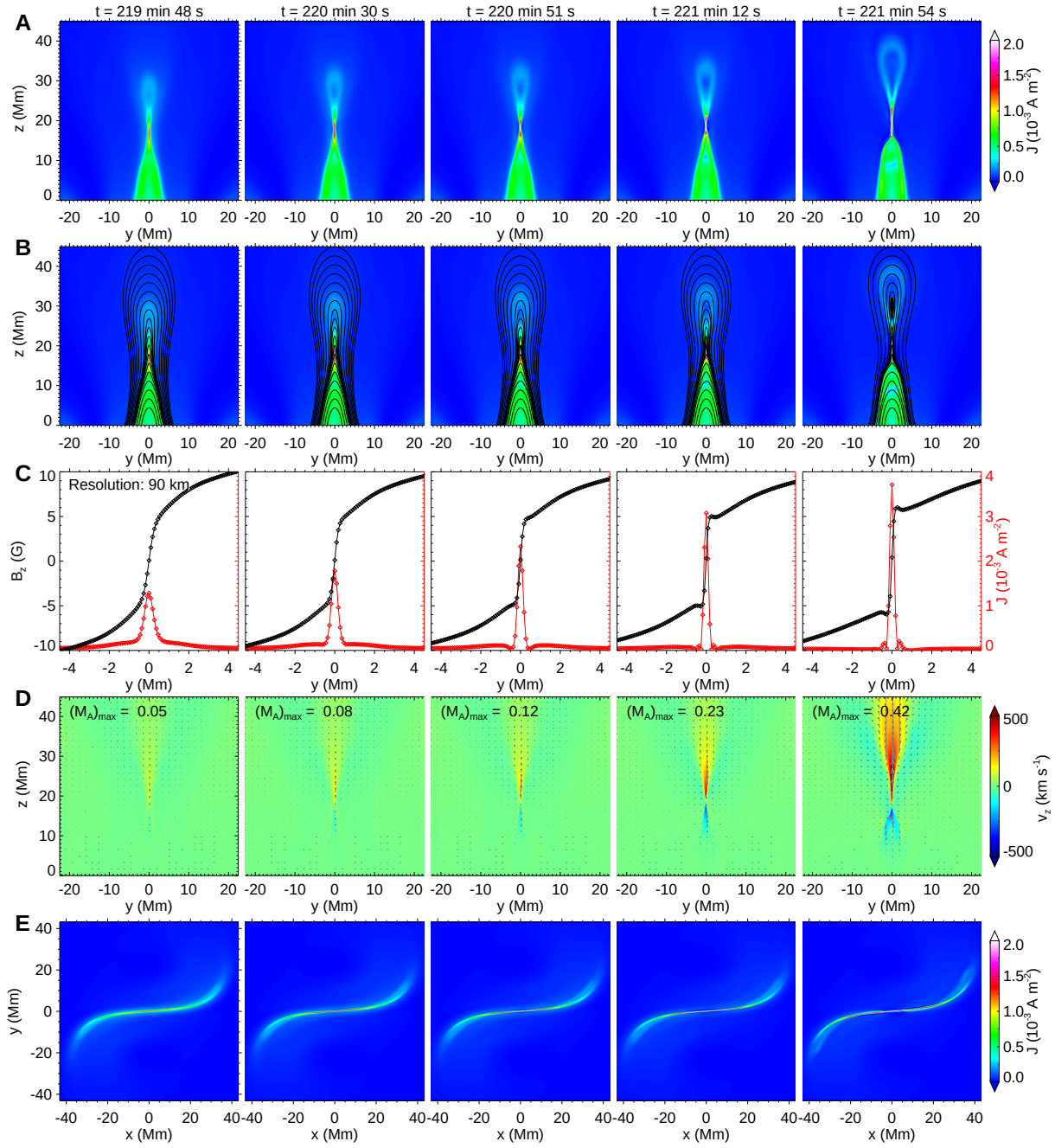

Figure 3: **Formation of CS and trigger of reconnection**. **(A)** Distribution of current density on the central vertical slice, i.e., the $x = 0$ slice. **(B)** Projection of magnetic field lines on the same cross section shown in **A**. **(C)** 1D profile of the magnetic field component B_z and current density J along a horizontal line crossing perpendicular to the CS center (i.e., the point with largest J). The diamonds denote values on the grid nodes. **(D)** Distribution of vertical velocity on the same cross section shown in **(A)**. The magnitudes of maximal Aflvénic Mach number are also denoted. **(E)** Horizontal slice of the current density crossing the center of the CS.

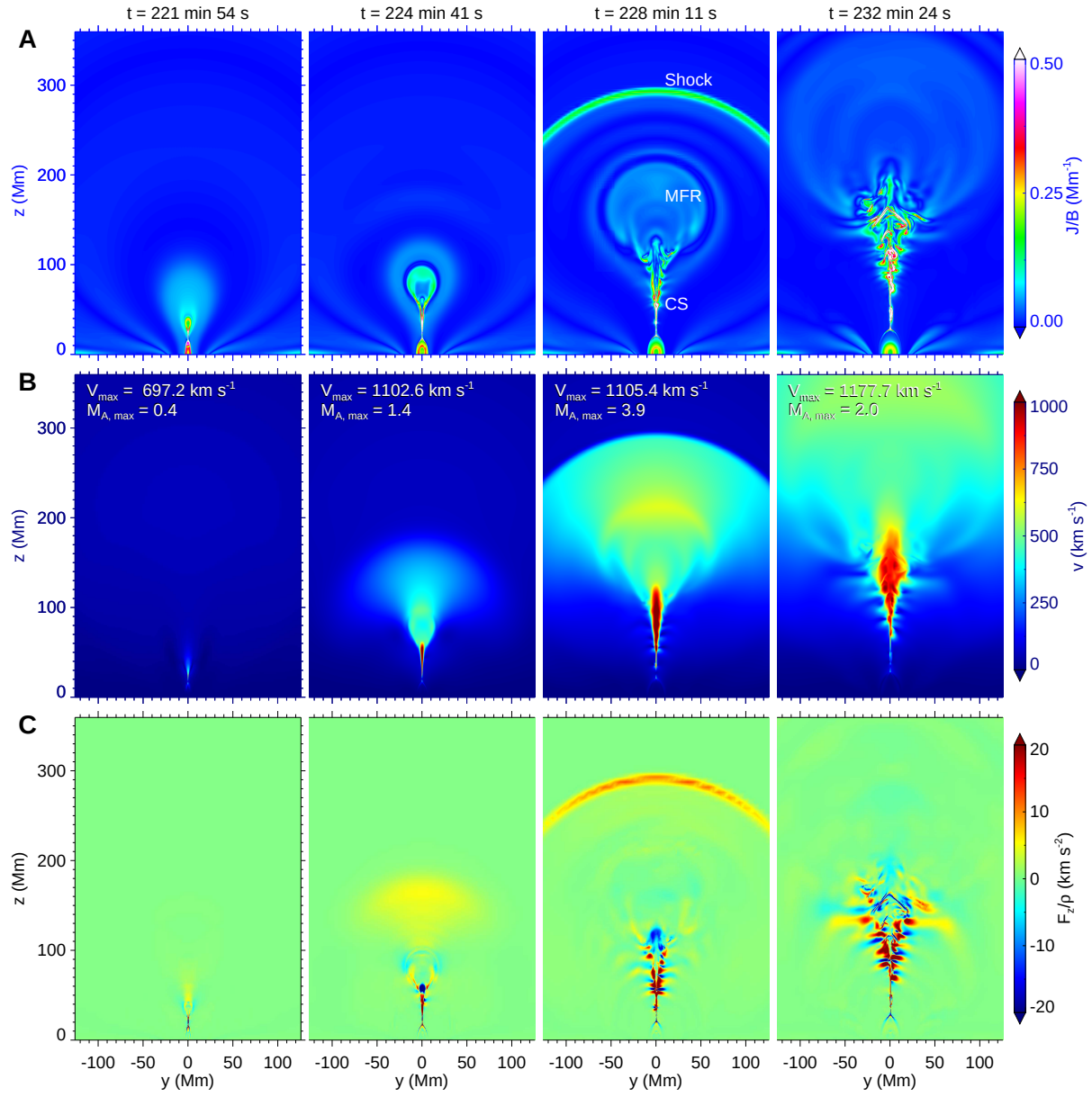

Figure 4: **Evolution of different parameters during the eruption shown in the central vertical slice**. **(A)** Current density J normalized by magnetic field strength B. **(B)** Magnitudes of velocity. The largest velocity and Aflvénic Mach number are also denoted. **(C)** The vertical component of Lorentz force F_z normalized by density ρ. Also see Supplementary Video 1 for a high-cadence evolution of the eruption process.

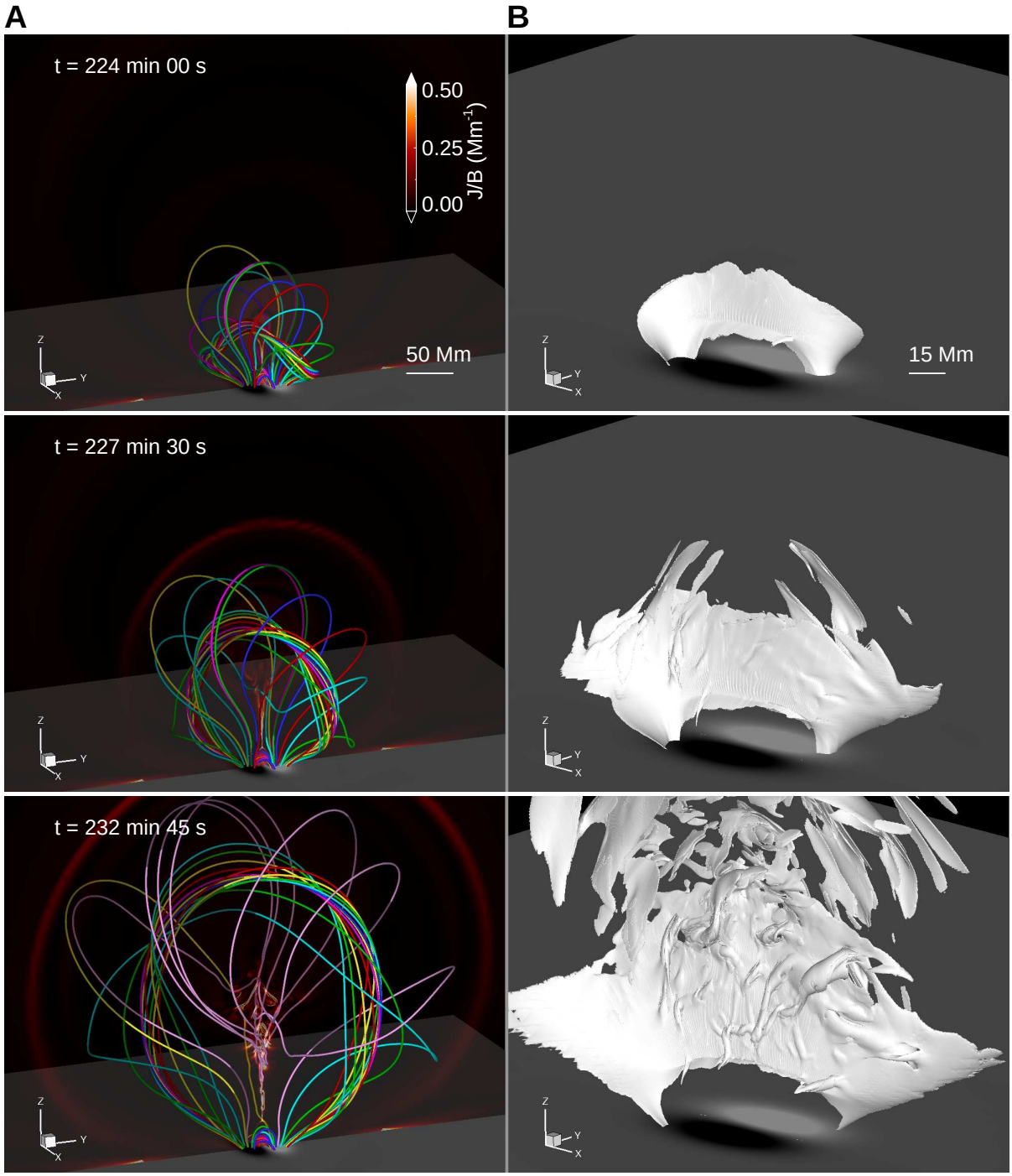

Figure 5: **Evolution of magnetic field lines and CS in 3D during the eruption. (A)** The magnetic field lines are shown by the thick colored lines, and **the colours are used for a better visualization of the different lines**. Note that the MFR is weakly twisted in its core but highly twisted in its envelope. The bottom surface is shown with distribution of magnetic flux. The vertical, transparent slice is shown with distribution of current density normalized by magnetic field strength, i.e., J/B. **(B)** The CS in 3D configuration is shown by iso-surface of $J/B = 0.5$ Mm^{-1}.

A Methods

A.1 Model equations

We numerically solve the full MHD equations in 3D Cartesian geometry by the advanced conservation element and solution element (CESE) method [52, 53, 54]. The MHD equations are given as

$$\begin{aligned} \frac{\partial \rho}{\partial t} + \nabla \cdot (\rho \mathbf{v}) &= 0, \\ \rho \frac{D\mathbf{v}}{Dt} &= -\nabla p + \mathbf{J} \times \mathbf{B} + \rho \mathbf{g} + \nabla \cdot (\nu \rho \nabla \mathbf{v}), \\ \frac{\partial \mathbf{B}}{\partial t} &= \nabla \times (\mathbf{v} \times \mathbf{B} - \eta \mu_0 \mathbf{J}), \\ \frac{\partial T}{\partial t} + \nabla \cdot (T\mathbf{v}) &= (2-\gamma) T \nabla \cdot \mathbf{v}, \end{aligned} \tag{1}$$

where $\mathbf{J} = \nabla \times \mathbf{B}/\mu_0$ and μ_0 is the magnetic permeability in a vacuum. In the momentum equation, a small kinetic viscosity ν is used for the purpose of keeping numerical stability during the very dynamic phase of the simulated eruptions. Specifically, the coefficient is given depending on the local spatial resolution Δ and time step Δt as $\nu = 0.05\Delta^2/\Delta t$, which corresponds to grid Reynolds number of 10. In the magnetic induction equation, the trigger of magnetic reconnection depends on the specific choice of magnetic diffusivity η. Here we avoid such a sensitivity by relying it solely on the numerical diffusion, that is, we set $\eta = 0$ in the magnetic induction equation. As such, we can minimize the resistivity and thus maximize the Lundquist number (with given spatial resolutions), since any finite value of η will result in larger resistivity than solely the numerical one. In this sense, magnetic reconnection occurs when a current layer is sufficiently narrow such that its width is close to the grid resolution, on which scale the numerical diffusivity takes effect. We have carefully estimated the value of numerical diffusivity $\eta_{\rm n}$ (see Methods A.6). In the energy (or temperature) equation, γ is the adiabatic index, and here for simplicity as we focus on the dynamics of the magnetic field, it is set as $\gamma = 1$ such that the energy equation describes an isothermal process.

A.2 Initial conditions

We start from a potential magnetic field with vertical component on the photosphere given by

$$B_z(x, y, 0) = B_0 e^{-x^2/\sigma_x^2} (e^{-(y-y_c)^2/\sigma_y^2} - e^{-(y+y_c)^2/\sigma_y^2}), \tag{2}$$

where $B_0 = 37.2$ G, $\sigma_x = 28.8$ Mm, $\sigma_y = \sigma_x/2$, and $y_c = 11.5$ Mm. Such magnetic configuration is similar to that used in reference [48]. As shown in Extended Data Fig. 1A, it mimics a bipolar solar AR of typical size, but the magnetic field strength is weaker than that of real sunspots by a least one order of magnitude to avoid a too heavy burden on computation.

The background atmosphere is stratified by solar gravity with density $\rho = 2.3 \times 10^{-15}$ g cm^{-3} at the bottom and an uniform temperature of $T = 10^6$ K (corresponding to sound speed of 110 km s^{-1}). Here we find that if using the real number of the solar gravity ($g_\odot = 274$ m s^{-2}), it results in a pressure scale height of $H_p = 43.8$ Mm, by which the plasma pressure and density decay with height much slower than the magnetic field. With the weak magnetic field strength we used, the plasma β will increase with height very fast to above 1, which is not realistic in the low corona. To make the pressure (and density) decrease faster in the lower corona, we modified the gravity by defining it as

$$g = \frac{k}{(1 + z/L)^2} g_\odot. \tag{3}$$

where $k = 5.7$ and $L = 76.8$ Mm. By this, we get a plasma $\beta < 1$ mainly within $z < 120$) Mm and the smallest value is 4×10^{-3} (Extended Data Fig. 1C). Note that with the energizing of the magnetic field by the shearing flow, the magnetic field inflates and its strength increases significantly in the upper volume, and the plasma β will decrease further. As can be seen in Extended Data Fig. 1, just prior to the eruption, the plasma β is much smaller than unity in the height up to 200 Mm, and the Alfvén speed higher than 1000 km s^{-1} within $z < 100$ Mm.

A.3 Boundary conditions

On the bottom boundary ($z = 0$), we apply the surface rotation flow (with $v_z = 0$) to add free magnetic energy to the initial potential field. To ensure that such flow will not modify the magnetic flux distribution B_z at the photosphere, the flow is incompressible and the streamlines coincide with the contour lines of B_z. Specifically, the surface velocity is set as

$$v_x = \frac{\partial \psi(B_z)}{\partial y}; v_y = -\frac{\partial \psi(B_z)}{\partial x}; \tag{4}$$

with ψ given by

$$\psi = v_0 B_z^2 e^{-(B_z^2 - B_{z,\max}^2)/B_{z,\max}^2} \tag{5}$$

where $B_{z,\max}$ is the largest value of the photosphere B_z, and v_0 is a constant for scale such that the maximum of the surface velocity is 4.4 km s^{-1}, close to the magnitude of typical flow speed in the photosphere (~ 1 km s^{-1}). The flow pattern is shown in Extended Data Fig. 1A and B. As the flow speed is smaller than the sound speed by two orders of magnitude and the local Alfvén speed by three orders, it stresses the corona magnetic field very slowly. Such flow mimics the frequently-observed sunspot rotation during evolution of ARs [55, 56, 57], and similar rotational flows have be employed in numerous numerical simulations for the same purpose of energizing pre-eruption fields but the magnitude is often larger than ours by an order [58, 59, 60, 61]. The energizing phase is linearly ramped on by a time of $t = 10.5$ s.

We fix plasma density on the bottom surface as being their initial, uniform value, because the surface flow is incompressible. Furthermore, as the velocity is prescribed there and B_z does not change, we only need to specify how the horizontal magnetic field evolves. To deal with this, many codes use simple linear extrapolation from the inner grid points, which, however, could falsely increase the magnetic energy (as shown in Supplementary Fig. 1). To minimize numerical errors introduced by any inappropriate treatment of the boundary conditions, we directly solve the ideal induction equation

$$\frac{\partial \mathbf{B}}{\partial t} = \nabla \times (\mathbf{v} \times \mathbf{B}) \tag{6}$$

on the bottom surface. By this we can self-consistently update the magnetic field and simulate the line-tied effect at the photosphere, which is essential for the success of the simulations in this type. Solving this equation is realized by second-order difference in space and forward difference in time. Specifically, on the bottom boundary (we do not use any ghost or guard cell), we first compute $\mathbf{v} \times \mathbf{B}$, and then use central difference in horizontal direction and one-sided difference (also 2nd order) in the vertical direction to compute the convection term $\nabla \times (\mathbf{v} \times \mathbf{B})$. We have further checked the accuracy with which the line-tied condition is implemented. To illustrate this, we traced the successive movements of footpoints of a single field line that is sheared through the area with the largest surface flow, which is shown in Supplementary Fig. 2. Since both footpoints of the field line convect with surface flow, we assume that the footpoint in the positive polarity (i.e., the $y > 0$ part) moves with flow exactly and trace the field line to its conjugated footpoint. If the line-tied condition is accurately implemented, the positions of the conjugated footpoint should be exactly the positions expected due to the applied flow. As shown in Supplementary Fig. 2, we traced the movement of the footpoints with a time cadence of 35 min until the onset of the eruption. As can be seen, the exact footpoints are almost excellently matched by the computed ones, except that the last one (i.e., $t = 6 \times 35$ min) has a finite, but still small, offset of about 0.5 Mm. Such a finite offset is more likely resulted by numerical errors in magnetic field line tracing rather than an actual slippage. In particular, as the field immediately prior to the eruption is strongly sheared, it forms a quasi-separatrix layer (QSL) in which the gradient of field-line mapping is extremely large, and small errors in field-line tracing can result in large offset. We note that a sufficient resolution of the driving surface is also important to avoid unwanted slipping of the field lines (see Methods A.8).

On the side and top boundaries, we fixed the plasma density, temperature and velocity. The tangential components of magnetic field are linearly extrapolated from the inner points, while the normal component is modified according to the divergence-free condition to avoid accumulation of numerical magnetic divergence near the boundaries. Furthermore, the simulation runs are stopped before the disturbance by the eruption reaches any of these boundaries to minimize the influence of these numerical boundaries on the computation.

It is worth noting that the time scale of the quasi-static, pre-eruption evolution is determined by the speed of the surface motion. Since the surface velocity we used

is still a few times (say, 5) larger in magnitude than typical photosphere flow, our simulated pre-flare evolution time, if compared with the realistic time scale, should be multiplied by a factor of 5, thus corresponding to roughly one day. On the other hand, the time scale of the eruption is controlled by the evolution in the coronal volume, and thus is not changed.

A.4 Grid setting and influence of eruption onset by different resolutions

The computational volume spans a sufficiently large box of approximately $(-370, -370, 0)$ Mm $< (x, y, z) < (370, 370, 740)$ Mm (where $z = 0$ represents the solar surface) such that during eruption the saturation of kinetic energy (i.e., the completion of CME acceleration) occurs prior to the moment when any disturbance reaching the side and top boundaries. The full volume is resolved by a block-structured grid with adaptive mesh refinement (AMR). The AMR is designed to automatically resolve with highest resolutions the narrow layers with strong currents (mainly in the low β region) as well as the regions where the magnetic field has a strong gradient (see Supplementary Video 8). Specifically, the base resolution is $\Delta x = \Delta y = \Delta z = \Delta = 2.88$ Mm, and we carried out four different runs with different highest resolutions, including $\Delta = 180$ km, 90 km, 45 km and 22.5 km (will be referred to RES0, RES1, RES2, and RES3 respectively, where RES1 is the main run). During the calculation any location with $J\Delta/B > 0.1$ will be refined to the highest resolution, and any location with strong magnetic field gradient or strong current, with criteria given by $|\nabla(B^2/2)|\Delta/\rho > 10$ and $|(\mathbf{B}\cdot\nabla)\mathbf{B}|\Delta/\rho > 10$ respectively, will also be refined. Furthermore, at the bottom boundary where the surface flow is applied, the resolution is forced to be no less than 180 km. If using uniform grids, to reach these resolutions requires grid numbers of 4096^3, 8192^3, 16384^3, and 32768^3, respectively, which is formidable.

The energy evolution curves from the different runs are compared in Supplementary Fig. 3. In all the runs, the energies evolve similarly, with pre-eruption to eruption clearly denoted by sharp transitions of energy curves and their changing rates. Note that the different resolutions do not change the evolution in the pre-eruption phase, i.e., the ideal MHD process, indicating that our simulation converges in the ideal MHD regime. However, the onset time of eruption in the runs is clearly different; it is postponed by about 100 s incrementally from run of RES0 to RES3. This is because, as we have mentioned before, the reconnection results from numerical diffusion when the pre-eruption CS is thin enough as close to the grid resolution. In this sense, the onset time of reconnection depends on the grid spacing, since with a smaller grid size a thinner CS can develop, and can sustain stronger current density (and thus more free energy), which needs more time to accumulate, and thus the onset of reconnection in the CS is postponed relative to runs with lower resolutions. This effect is exactly shown in Supplementary Fig. 3 and Supplementary Video 2. With the resolution increased from RES0 to RES3, the thickness

of the CS at the eruption onset decreases from approximately 500 km to 50 km, and correspondingly, the peak current density in the CS increases proportionally from approximately 2×10^{-3} A m^{-2} to 14×10^{-3} A m^{-2}. We note that there is a clear link between the field at the eruption onset and the corresponding open-field configuration by comparing the peak current density and the maximal current density of the open field discretized with the same grid resolution. For instance, as can be seen in Extended Data Fig. 3 which shows the open field discretized with resolution of 90 km, the current density in the CS is not infinite but rather changes with height and at approximately $z = 10$ Mm it reaches the maximum of 13×10^{-3} A m^{-2}. This value is close to triple of the peak current density ($\sim 4 \times 10^{-3}$ A m^{-2}) in the CS of RES1 run, which is consistent with the fact that the CS thickness in RES1 run is approximately triple of 90 km. The fast reconnection always starts when the CS thins down to about $2 \sim 3$ grid spacings, independent of how small the grid spacing is, and once the reconnection kicks in, the eruption starts. These tests with different resolutions confirm again that reconnection plays the key role in triggering the eruption. It is expected that by using further higher resolutions the CS will be thinner and the current density can increase accordingly. If needed (though formidable in computation), it could be even thinned down to the kinetic scale, i.e., the ion gyro-radius or inertial length, where the MHD approximation fails, as the current density may exceed the threshold of a microscopic instability and anomalous resistivity arises to trigger reconnection [62].

Once the eruption is triggered, it evolves rather differently on small scales in the different runs, since with the higher resolution, the earlier the tearing instability can be triggered, and the more complex the turbulent reconnecting CS will be (Supplementary Video 9), and thus there are more fluctuations seen in the curves of energy evolutions (Supplementary Fig. 3B and C).

A.5 Quasi-static formation of CS

A key aspect of our 3D simulation is that the CS forms in a quasi-static way. Prior to the eruption onset, the horizontal flow on two sides of the current layer converges to it and plays the role of thinning the current layer to CS (Supplementary Video 2C and F). As the converging motion is directly driven by the surface shearing motion, the converging speed, i.e., the thinning speed of the current layer, is on the same order of the surface flow speed, which is several km s^{-1} (for instance, see Supplementary Fig. 4 for the runs of RES2 and RES3). This is distinguished from other 3D simulations of eruption where the central CS accounting for the flare reconnection is formed in a dynamic way. For example, in the MFR-based models, the CS forms after the rise of the erupting MFR, which forces the oppositely directed field lines below the MFR to approach each other quickly. Similarly, in the breakout model, firstly the reconnection begins at the null and triggers a feedback between the expansion of the inner sheared arcades and the breakout reconnection, making the system run into a dynamic phase, and then the main flare CS forms.

In numerical simulations, it is much more challenging to form a CS in a quasi-

static way than in a dynamic way (especially in the absence of magnetic topological separatries such as the magnetic null point). This is because, a current layer will diffuse and broaden by the numerical diffusion $\eta_{\rm n}$. Say, for a thin current layer with thickness of l, it will diffuse (or broaden) with a speed of $v_{\rm d} = \eta_{\rm n}/l$ in the absence of inflow [63]. The current layer can only be thinned by a inflow v_i larger than the diffusing speed, i.e., $v_i > v_{\rm d}$. This means to form a CS with thickness l, one must have $\eta_{\rm n} < v_i l$. In the dynamic formation of CS, this can be easily fulfilled since the inflow speed v_i is sufficiently large to exceed the diffusion speed $v_{\rm d}$. In our simulation, the inflow v_i is as slow as several km s^{-1}. For instance, in our RES3 run, $l \approx 60$ km, $v_i \approx 3$ km s^{-1}, which requires the numerical diffusivity $\eta_{\rm n} < v_i l \approx 180$ km^2 s^{-1}. Thus only with a sufficiently small numerical diffusivity can the CS form in a quasi-static way. Note that the quasi-static formation of CS is directly related to degree of the magnetic shear and free energy storage. If the numerical diffusivity is too large, the CS cannot form since magnetic free energy diffuses faster than the injection rate from the bottom surface. Such a numerical effect is also seen in a previous 2D simulation [64], and this might be the key reason why early simulations fail to reproduce the runaway tether-cutting model in fully 3D since they have too large numerical diffusion to form a thin CS in the pre-eruption quasi-static evolution. As a result, the numerical resistivity takes effect much earlier before the CS forms, and the resulted reconnection, which is slow, will readily build up MFR in the pre-eruption phase. Such an MFR formation process, aided with surface converging motion (or flux cancellation), has been commonly seen in earlier 3D simulations [48, 13]. This also explains why many 3D numerical simulations tend to support the MFR-based eruption scenarios. However, we note that the quasi-static formation of CS is a key process in the pre-eruption evolution, and besides, it is also essential for explaining confined flares, in which only flare emission is observed but without noticeable movement of coronal loops [65], indicating that CS thinning and the subsequent reconnection are not driven by dynamic evolution.

A.6 Estimation of effective magnetic diffusivity and Lundquist number

In the solar corona, the magnetic diffusivity as derived from the Spitzer resistivity [66] is $\eta \approx 1$ m^2 s^{-1}, and at a typical length scale, e.g., $L = 10$ Mm, and Alfvén speed of $v_{\rm A} = 10^3$ km s^{-1}, the coronal environment has extremely large Lundquist number of $S = Lv_{\rm A}/\eta \approx 10^{13}$. Thus fast reconnection only occurs when a CS is sufficiently thin, e.g., with thickness of a few to tens of meters. Although it is prohibitive to reach such a high Lundquist number in numerical simulations of large-scale eruptions, we attempted to mimic the coronal conditions as much as we can. Here we estimate the values of the numerical diffusivity $\eta_{\rm n}$ and the corresponding Lundquist number in the runs with different resolutions. Since the eruption is triggered by reconnection, the different values of actual diffusivity will naturally result in different onset times of reconnection and thus eruption. That is,

the larger the diffusivity is, the earlier the eruption is triggered. As our MHD code has a second-order accuracy, the numerical diffusivity decreases with resolution by a power of two, i.e., $\eta_{\rm n} \propto \Delta^2$. For example, in RES0 the numerical diffusivity is four times of that in RES1. If the onset time of eruption in RES1 using a particular value of η coincides with the eruption onset time in RES0 without explicit diffusivity, then we can estimate that $\eta = 3\eta_{\rm n}$ in RES1, as such the total diffusivity in RES1 is $4\eta_{\rm n}$, which equals to the numerical diffusivity in RES0.

Thus, to quantify the $\eta_{\rm n}$ in RES1, we run a series of tests with RES1 using different values of explicit diffusivity η. Since this needs many runs, we speedup the bottom boundary flow by 5 times such that the largest speed is 22 km s^{-1} to save the computing time. By this speed, it is still a slow quasi-static driving of the coronal field, though the pre-eruption evolution is faster than that in our main run. Supplementary Fig. 5A shows the energy curves for the run with $\eta = 0$, which is very similar to those of the main run shown in Fig. 2, except that the timing is different and the pre-eruption kinetic energy is somewhat larger. Then in Supplementary Fig. 5B, we compare the RES1 using a sequence of η with the RES0 using $\eta = 0$ by plotting the changing rate of kinetic energy from the pre-eruption to eruption phases. Clearly, the larger the diffusivity is, the earlier the eruption is triggered. From these tests, we can estimate the numerical diffusivity with RES1 to be $\eta_{\rm n} \approx 1.3 \times 10^{-3}$ Mm^2 s^{-1} or 1300 km^2 s^{-1}, and thus the Lundquist number $S = Lv_{\rm A}/\eta_{\rm n} \approx 1 \times 10^4$, where $L = 10$ Mm is the vertical length scale of the CS immediately prior to eruptions and $v_{\rm A} = 10^3$ km s^{-1} is the typical Alfvén speed around the CS. Accordingly, the numerical diffusivity in runs of RES2 and RES3 are approximately 300 km^2 s^{-1} and 80 km^2 s^{-1} (the latter is consistent with aforementioned requirement for CS formation in Methods A.5, i.e., $\eta_{\rm n} < v_i l =$ 180 km^2 s^{-1}), and the Lundquist numbers are 4×10^4 and 1.6×10^5, respectively. The Lundquist numbers further increase with the length of the CS, which grows as the eruption goes on. We note that the Lundquist numbers in our fully 3D simulations are comparable to and even larger than values used in 2D simulations of the similar type [46, 47, 64]. If considering to extrapolate our values to the real coronal conditions, we would needs a grid resolution of $\Delta \approx \Delta_{\rm RES3}/10^4$, on which the effective diffusivity can then be $\eta = \eta_{\rm RES3}/10^8 \approx 1$ m^2 s^{-1}, the Lundquist number $S = S_{\rm RES3} \times 10^8 \approx 10^{13}$ and the CS thickness $l \sim 3\Delta \approx 7$ m, which are all consistent with the classical values derived from the Spitzer resistivity.

A.7 Magnetic reconnection rate and indication for fast reconnection

In Supplementary Fig. 6A, we compare the reconnection rates, measured by the inflow Alfvénic Mach number, of the 4 runs with increasing resolution (or Lundquist number). As the highest resolution run (RES3) stops earlier when the reconnection lasts for about 3 minutes, we thus compare the reconnection rates averaged in the initial 3 minutes for all the runs. All the runs show fast reconnection rate of ~ 0.05,

which is weakly dependent on the Lundquist number. From RES0 to RES2, the reconnection rate decreases slightly while for RES3 it increases a little bit again.

The reconnection in our simulations starts with the Petschek type, i.e., with onset at a single X-point. This is mainly because the numerical resistivity in our code actually mimics an anomalous resistivity since it is almost negligible in the smooth field region and becomes effective (or turns on) only when the current density exceeds a critical value such that the thickness of CS is close to the grid size. It is similar to using an explicit form of resistivity that depends sensitively on the local current density [67], which can lead to the Petschek-type reconnection. Furthermore, the CS is formed with very non-uniform current density and thickness along its length (Supplementary Fig. 7), i.e., during the formation of CS, the current density grows much faster at its peak-value point than elsewhere, and thus the reconnection should be first triggered at the point with the largest current density. Such inhomogeneity is inherent to the 3D nature of the magnetic configuration.

Our scaling experiments with the 4 different resolutions indicate that the CS can be further thinned (especially at the point of peak value of current density) with higher resolutions, even possibly down to the scale at which the micro-instability is triggered and creates true anomalous resistivity for fast Petschek reconnection [62]. But before this, the Lundquist number of the CS should be well above the critical value ($\sim 10^4$) for the nonlinear plasmoid instability, which will also be triggered and realize again fast reconnection nearly independent of Lundquist number [42, 43]. Our simulation indicates this clearly since the plasmoids emerge earlier and their number grows faster in the runs with higher resolutions (Supplementary Video 9). Additionally, the turbulence as excited by the plasmoid-mediated reconnection, can also enhance the reconnection rate [68, 69]. Supplementary Fig. 6B and C show the evolution of the maximum value of velocity in each run, and the comparison of different resolutions show that the impulsiveness of plasma acceleration increases and the turbulent fluctuation starts sooner as the resolution increases. Especially in RES3, the turbulence is induced within nearly 1 minute after the reconnection starts, and this explains partially why the reconnection rate of RES3 exceeds RES2.

Since all these mechanisms as shown in our simulation, namely the Petscheck-type reconnection, the plasmoid instability as well as the induced turbulence, can produce fast reconnection with rate scaling weakly on Lundquist number, there is a strong indication of fast reconnection with much higher resolutions, or equivalently, much higher Lundquist numbers, eventually reaching the realistic values of $\sim 10^{13}$ in the corona. However, the very details on how reconnection works at such high Lundquist number and small scales are unknown as it is prohibitive to simulate in current computations, and moreover they are related to the complex coupling between the MHD and kinetic scales, which is beyond the scope of this work.

A.8 A "failed" simulation with inaccurate boundary conditions

As aforementioned, a sufficiently high resolution at the bottom boundary is also required to accurately implement the line-tied boundary condition, and further to form sufficiently thin CS. To show this, we run an experiment with the highest resolution of 90 km (same as RES1) to resolve the current layer but using a four times lower resolution (i.e., 720 km with respect to 180 km in the main run) at the bottom boundary. As can be seen in Supplementary Fig. 8A, this run failed to produce an eruption, as no impulsive release of magnetic energy accompanied with fast rise of kinetic energy is seen. In contrast to the high-resolution run, there is a considerable amount of magnetic energy loss in the surface driving process. This is because the line-tying condition is not accurately achieved (see Supplementary Fig. 8B) in the lower resolution due to numerical errors. Consequently, the field lines slip backward and are unable to obtain the amount of shear as needed for the CS formation. If putting the two negative factors together, i.e., the MHD code has a large numerical diffusion and the line-tied boundary condition is not accurately implemented, it is very likely that the magnetic energy eventually saturates once the net energy injection rate from the bottom surface is totally cancelled by the diffusion rate. Therefore eruption can not happen even if the surface shearing is continuously applied.

A.9 Evolution of magnetic topology and formation of MFR

The magnetic topology is a simple arcade until the eruption onset and, once reconnection begins, it transforms to complex one having a highly twisted MFR formed during the eruption. To reveal the variation of magnetic topology, we inspected the distribution and evolution of two parameters, the magnetic squashing degree and magnetic twist number, which are commonly used for study of 3D magnetic fields and their dynamics [70, 71, 72, 73, 74, 75]. The magnetic squashing degree Q quantifies the gradient of magnetic field-line mapping with respect to their footpoints, and it is helpful for searching QSLs of magnetic fields [76], which can have extremely large values of Q (e.g., $\geq 10^5$) and are preferential sites of magnetic reconnection. Specifically, for a field line starting at one footpoint (x, y) and ending at the other footpoint (X, Y) where X and Y are both functions of x and y, the squashing degree Q associated with this field line is given by [76]

$$Q = \frac{a^2 + b^2 + c^2 + d^2}{|ad - bc|} \tag{7}$$

where

$$a = \frac{\partial X}{\partial x}, \quad b = \frac{\partial X}{\partial y}, \quad c = \frac{\partial Y}{\partial x}, \quad d = \frac{\partial Y}{\partial y}. \tag{8}$$

The magnetic twist number T_w [77] is defined for a given (closed) field line by taking integration of $T_w = \int_L \mathbf{J} \cdot \mathbf{B}/B^2 dl/(4\pi)$ along the length L of the field line between two conjugated footpoints on the photosphere. Note that T_w is not identical to the classic winding number of field lines about a common axis, but an approximation of the number of turns that two infinitesimally close field lines wind about each other [74].

Supplementary Fig. 9 and Supplementary Video 10 show evolution of magnetic squashing degree Q on the central vertical slice, as well as both the Q, T_w and current density J on the bottom surface, respectively. As can be seen, the formation of CS is accompanied by the formation of corresponding QSLs. Initially the distribution of Q is rather smooth, and with narrowing of the current layer, there is an evident increasing of Q (reaching $\sim 10^5$) in two thin strips of J shape, i.e., QSLs, on either side of the PIL on the bottom surface. These QSLs correspond to the intersection of the CS with the photosphere, and thus two thin ribbons of enhanced current density are also seen, co-spatial with the QSLs. With onset of the reconnection, the two J-shaped QSLs and the current ribbons on the bottom surface evolve rapidly, which corresponds to the apparent motion of footpoints of the field lines that were undergoing reconnection, or simply the motion of observed flare ribbons [78, 73, 79].

In the early phase, the reconnection is fully a 3D manner with a strong guide field component (i.e., B_x) because joining in the reconnection is mainly the strongly-sheared, low-lying flux. While in the later phase, it transfers into a quasi-2D manner, which consumes mainly the large-scale, overlying flux that is weakly sheared. Such transition is clearly manifested by the fast elongation of the arms of the J-shaped QSLs along the direction of the PIL on the bottom surface, which agrees with observed elongation of flare ribbons [80]. Specifically, the arm of the QSL in the north (south) of the PIL spreads to the left (right), and as a result, the observed two ribbons naturally exhibit an evolution pattern of strong-to-weak shear [81]. As the eruption proceeds, more and more magnetic fluxes reconnect, and consequently, the two J-shaped QSLs continuously separate with each other, in agreement with the well-known separation motion of two flare ribbons. At the end of the simulation, they have swept to near the center of each magnetic polarity (or the umbra of the sunspots). On the central vertical slice, the QSLs intersect with each other, developing into an X shape, which is referred to a hyperbolic flux tube (HFT) [76], and the intersection X point is essentially the main reconnection site (in analogy to the null point in a 2D X-shaped reconnection configuration). As the reconnection proceeds, the X point of the HFT rises upward progressively with the cusp region below expanding.

Starting from the hooks of the J-shaped QSLs, twisted magnetic flux (as indicated with $T_w < -2$) begins to form owing to the tether-cutting reconnection, which creates long field lines connecting the far ends of the two pre-reconnection sheared field lines. With the twisted flux accumulated through the continuation of reconnection, the areas occupied by the footpoints of the highly twisted field lines at the hooks expand. Consequently, the hook of each J-shaped QSL continuously extends inward until it reaches the arm, forming a closed curve encircling the highly

twisted flux (see the panels of $t = 226$ min 06 s). Such a transition of QSLs ought to be observed as flare ribbons that gradually forms close rings [22]. Accordingly, as can be seen in the vertical cross section, the QSLs form a closed tear-drop shape connecting the HFT. Thus, in magnetic topology, at this moment the MFR is fully separated with its surrounding magnetic field by the QSLs [82, 83, 84]. Interestingly, this moment is close to the peak time of the magnetic energy release rate and the kinetic energy increasing rate. We note that the distribution of magnetic twist degree is rather inhomogeneous, and the most strongly twisted flux is seen around the boundary of the MFR, meaning that the newly-formed MFR has weaker twisted axis wrapped by stronger winding field lines. It is also worthy noting that the details of the QSLs associated with the MFR become extremely complex in the later phase with many fast evolving small structures (see Supplementary Video 10) because of the turbulence excited in the reconnection. The current ribbons also show small evolving kernels, which might correspond to the observed bright kernels or knots within flare ribbons [85].

A.10 Analysis for the driver of the eruption

Once the MFR is formed, it can be subject to the torus instability if its axis reaches a height where the external (or strapping) magnetic field decays fast enough with height such that the hoop force of the MFR exceeds the strapping force in its subsequent expansion. Thus, the torus instability can occur regardless of whether the MFR is formed in equilibrium or dynamically. To check whether the MFR formed in our simulation is affected by such instability in its acceleration, we calculate the decay index of the external field at the time when the MFR first forms, which is $t = 221$ min 33 s (in RES1). Since it is only B_y that actually straps the MFR, the decay index is defined as $n = -d\ln(-B_y)/d\ln(z)$. Here the external field B_y consists of two components by two different sources of currents: one is the field generated by current below the bottom surface, i.e., the potential field; the other is the field generated by current above the surface but below the MFR, which is mainly the CS. The reason why the latter should be considered is that, as the current in the CS follows in the same direction as that of the MFR, it attracts the MFR and thus prevents the MFR's outward expansion by enhancing the external field overlying the MFR. However, it is difficult to separate the current in the CS with that of the MFR as the coronal current distributes continuously from the CS to the MFR. To give a reasonable approximation of the external field, we use the total magnetic field B_y at an earlier time ($t = 217$ min) than the eruption onset, since at that moment the MFR is not yet formed (thus there is no current of MFR), and meanwhile the current in the corona is close to that in the CS below the MFR at the onset time.

The results are given in Extended Data Fig. 2. For comparison, we also plot the field profile and decay index at the initial time as well as the time when the MFR first forms. It shows that, at the onset of eruption, the apex of the newly formed MFR is located at a height of 25 Mm, much lower than the critical height of torus instability ($\sim$ 75 Mm), i.e., the height at which the decay index of the external

field reaches the canonical threshold of 1.5. This suggests that the torus instability does not occur at the onset of the eruption. We note that the current in the CS below the MFR contributes a large portion to the external field, which is thus much stronger than the initial potential field (by at least several times at height above 50 Mm). Therefore, a simple approximation of the external field by the potential field, as often used in observational studies, might significantly underestimate the actual value if the current below the MFR is strong. We also note that the profile of decay index at the time when the MFR first forms (the blue line) is very close to the one (the pink line) at $t = 217$ min before the MFR forms, because the current in the MFR at its initial formation is much weaker than that in the lower CS, and thus contributes very minimally to the total overlying field.

We further analyze the process of the MFR acceleration during the eruption. In Supplementary Fig. 10 (and Supplementary Video 7), we show the dynamics of a sequence of magnetic field lines that undergo reconnection and become part of the MFR. By following the movement of each field line, one can clearly see how the MFR is accelerated. After each field line approaches the CS and reconnects, its middle point (i.e., the intersection point of the field line with the central cross section) is immediately accelerated upward from nearly 0 to 500 $\sim$ 1000 km s^{-1}, close to the local Alfvén speed. Such acceleration is realized through the slingshot effect of reconnection by the upward magnetic tension force (Supplementary Fig. 11). It is extremely rapid, reaching up to $\sim$ 50 km s^{-2}, and is accomplished in a few tens of seconds within a rather lower height (below 50 Mm, Supplementary Fig. 10D). Then the field line is decelerated briefly because it relaxes quickly from upward to downward concave one, during which the tension force changes sign.

The high-speed magnetic flux is also decelerated as it pushes the field lines ahead in the MFR, which results in a downward magnetic pressure force for a brief interval immediately after the reconnection (Supplementary Fig. 11). Specifically, the field lines that join the MFR in different time show different behaviors. The very early reconnected field line obtained relatively lower speed by the slingshot effect (for instance, the field line 1 shown in Supplementary Fig. 10 obtains 400 km s^{-1}), while the later-reconnected ones gain higher and higher speed (e.g., 500 km s^{-1} for field line 2, 700 km s^{-1} for field line 3, and so on) with the rise of the reconnection rate (and the energy conversion rate) until its peak time ($t = 227$ min). Therefore, the early reconnected one is pushed upward by the later reconnected, faster ones from below, and thus is accelerated, and this process occurs one-by-one, seamlessly, for each field line that joins the MFR in time sequence. This secondary phase of acceleration of the field lines, with values of $\sim$ 1 km s^{-2}, is much slower than the initial one by the slingshot effect of reconnection, and it continues much longer until the reconnection rate reaches its peak (see especially the field line 1). Eventually, all the field lines approach a nearly uniform speed of 500 $\sim$ 600 km s^{-1} at which the MFR erupts as a whole (Supplementary Fig. 10).

Thus, for each field line of the MFR, the initial acceleration by reconnection plays the key role in determining its final speed, and moreover, the speed achieved directly from reconnection is much higher than the final erupting speed of the MFR

(except the very early reconnected ones). This analysis clearly suggests that the reconnection with its slingshot effect is the central engine of MFR acceleration, or in other words, most of the work for the MFR acceleration is done by the upward tension force as a result of the reconnection. The bursty nature of such acceleration and its accomplishment within a rather lower height is inherent to the reconnection of the strong field. This is unlike MFR acceleration through torus instability, which should last for a larger height and a longer time after the MFR runs across the threshold height, and thus work less impulsively than the reconnection.

However, whether the MFR, after being accelerated by the reconnection, can escape into the solar wind as a CME, should also depend on the strength of the overlying field relative to the core field as well as its decay rate with height. Our simulation shows that in the later phase, i.e., after the peak time of energy conversion rate, the hoop force of the MFR (approximately the magnetic pressure force) approximately balances the strapping force (approximately the tension force, see Supplementary Fig. 11), indicating that the MFR is close to torus instability. Such behavior is relevant to details of the overlying or envelope field of the sheared core. We anticipate that a stronger overlying field configuration might render the eruption failed, if the strapping force exceeds the hoop force of the MFR. With a further stronger overlying field, the reconnection might be slowed and terminated very early by the strong confinement, simply producing a confined flare without formation of MFR. On the contrary, a weaker (and faster decaying) overlying field could allow the MFR to run into torus instability, which will lead to even faster eruption. Similarly, if the overlying field consists of a multipolar configuration with a null point, as required in the breakout model, reconnection at the null also provides an efficient way to weaken the overlying field, thus facilitating the MFR to escape.

References

[1] Fleishman, G. D., et al. Decay of the coronal magnetic field can release sufficient energy to power a solar flare. *Science*, 367, 278–280 (2020).

[2] Priest, E. R. & Forbes, T. G. The magnetic nature of solar flares. *Astron. & Astrophys. Rev.*, 10, 313–377 (2002).

[3] Forbes, T. G., et al. CME Theory and Models. *Space Sci. Rev.*, 123, 251–302 (2006).

[4] Shibata, K. & Magara, T. Solar flares: magnetohydrodynamic processes. *Living Rev. Sol. Phys.*, 8, 6 (2011).

[5] Chen, P. F. Coronal mass ejections: models and their observational basis. *Living Rev. Sol. Phys.*, 8, 1 (2011).

[6] Schmieder, B., Démoulin, P. & Aulanier, G. Solar filament eruptions and their physical role in triggering coronal mass ejections. *Advances in Space Research*, 51, 1967–1980 (2013).

[7] Aulanier, G. The physical mechanisms that initiate and drive solar eruptions. *IAU Symposium*, 300, 184–196 (2014).

[8] Janvier, M., Aulanier, G. & Démoulin, P. From coronal observations to MHD simulations, the building blocks for 3D models of solar flares (invited review). *Sol. Phys.*, 290, 3425–3456 (2015).

[9] Lin, J., et al. Review on current sheets in cme development: theories and observations. *Space Sci. Rev.*, 194, 237–302 (2015).

[10] Kliem, B. & Török, T. Torus instability. *Phys. Rev. Lett.*, 96, 255002 (2006).

[11] Török, T. & Kliem, B. Confined and ejective eruptions of kink-unstable flux ropes. *Astrophys. J. Lett.*, 630, L97–L100 (2005).

[12] Fan, Y. & Gibson, S. E. Onset of coronal mass ejections due to loss of confinement of coronal flux ropes. *Astrophys. J.*, 668, 1232–1245 (2007).

[13] Aulanier, G., Török, T., Démoulin, P. & DeLuca, E. E. Formation of torus-unstable flux ropes and electric currents in erupting sigmoids. *Astrophys. J.*, 708, 314–333 (2010).

[14] Amari, T., Canou, A., Aly, J.-J., Delyon, F. & Alauzet, F. Magnetic cage and rope as the key for solar eruptions. *Nature*, 554, 211–215 (2018).

[15] Antiochos, S. K., DeVore, C. R. & Klimchuk, J. A. A model for solar coronal mass ejections. *Astrophys. J.*, 510, 485–493 (1999).

[16] Aulanier, G., DeLuca, E. E., Antiochos, S. K., McMullen, R. A. & Golub, L. The topology and evolution of the Bastille Day flare. *Astrophys. J.*, 540, 1126–1142 (2000).

[17] Lynch, B. J., Antiochos, S. K., DeVore, C. R., Luhmann, J. G. & Zurbuchen, T. H. Topological evolution of a fast magnetic breakout CME in three dimensions. *Astrophys. J.*, 683, 1192–1206 (2008).

[18] Wyper, P. F., Antiochos, S. K. & DeVore, C. R. A universal model for solar eruptions. *Nature*, 544, 452–455 (2017).

[19] Patsourakos, S., et al. Decoding the pre-eruptive magnetic field configurations of coronal mass ejections. *Space Sci. Rev.*, 216, 131 (2020).

[20] DeVore, C. R. & Antiochos, S. K. Dynamical formation and stability of helical prominence magnetic fields. *Astrophys. J.*, 539, 954–963 (2000).

[21] Wang, H., et al. Witnessing magnetic twist with high-resolution observation from the 1.6-m New Solar Telescope. *Nat. Commun.*, 6, 7008 (2015).

[22] Wang, W., et al. Buildup of a highly twisted magnetic flux rope during a solar eruption. *Nat. Commun.*, 8, 1330 (2017).

[23] Ugarte-Urra, I., Warren, H. P. & Winebarger, A. R. The Magnetic Topology of Coronal Mass Ejection Sources. *Astrophys. J.*, 662, 1293–1301 (2007).

[24] Moore, R. L. & Labonte, B. J. The filament eruption in the 3B flare of July 29, 1973 - Onset and magnetic field configuration. *IAU Symposium*, 91, 207–210 (1980).

[25] Moore, R. L. & Roumeliotis, G. Triggering of eruptive flares - destabilization of the preflare magnetic field configuration. *Lecture Notes in Physics, Berlin Springer Verlag*, 399, 69 (1992).

[26] Moore, R. L., Sterling, A. C., Hudson, H. S. & Lemen. J. R. Onset of the magnetic explosion in solar flares and coronal mass ejections. *Astrophys. J.*, 552, 833–848 (2001).

[27] Schrijver, C. J. A Characteristic Magnetic Field Pattern Associated with All Major Solar Flares and Its Use in Flare Forecasting. *Astrophys. J.*, 655, L117–L120 (2007).

[28] Toriumi, S. & Wang, H. Flare-productive active regions. *Living Rev. Sol. Phys.*, 16, 3 (2019).

[29] Emslie, A. G., et al. Global energetics of thirty-eight large solar eruptive events. *Astrophys. J.*, 759, 71 (2012).

[30] Zhang, J., Dere, K. P., Howard, R. A., Kundu, M. R. & White, S. M. On the Temporal Relationship between Coronal Mass Ejections and Flares. *Astrophys. J.*, 559, 452–462 (2001).

[31] Zhang, J. & Dere, K. P. A Statistical Study of Main and Residual Accelerations of Coronal Mass Ejections. *Astrophys. J.*, 649, 1100–1109 (2006).

[32] Cheng, X. et al. Initiation and Early Kinematic Evolution of Solar Eruptions. *Astrophys. J.*, 894, 85 (2020).

[33] Aly, J. J. How much energy can be stored in a three-dimensional force-free magnetic field? *Astrophys. J.*, 375, L61–L64, (1991).

[34] Sturrock, P. A. Maximum energy of semi-infinite magnetic field configurations. *Astrophys. J.*, 380, 655-659, (1991).

[35] Petschek, H. E. *Magnetic Field Annihilation*, 50, 425 (1964).

[36] Linker, J. A., et al. Flux cancellation and coronal mass ejections. *Phys. Plasmas*, 10:1971–1978, (2003).

[37] Amari, T., Luciani, J. F., Aly, J. J., Mikic, Z. & Linker, J. Coronal Mass Ejection: Initiation, Magnetic Helicity, and Flux Ropes. I. Boundary Motion-driven Evolution. *Astrophys. J.*, 585, 1073–1086 (2003).

[38] Török, T., et al. Sun-to-Earth MHD Simulation of the 2000 July 14 Bastille Day Eruption. *Astrophys. J.*, 856, 75 (2018).

[39] Wang, H., Qiu, J., Jing, J. & Zhang, H. Study of Ribbon Separation of a Flare Associated with a Quiescent Filament Eruption. *Astrophys. J.*, 593, 564–570 (2003).

[40] Hinterreiter, J., Veronig, A. M., Thalmann, J. K., Tschernitz, J. & Pötzi, W. Statistical Properties of Ribbon Evolution and Reconnection Electric Fields in Eruptive and Confined Flares. *Sol. Phys.*, 293, 38 (2018).

[41] Yan, X. L., et al. Successive X-class Flares and Coronal Mass Ejections Driven by Shearing Motion and Sunspot Rotation in Active Region NOAA 12673. *Astrophys. J.*, 856, 79 (2018).

[42] Bhattacharjee, A., Huang, Y. M., Yang, H. & Rogers, B. Fast reconnection in high-Lundquist-number plasmas due to the plasmoid instability. *Phys. Plasmas*, 16, 112102 (2009).

[43] Huang, Y. M. & Bhattacharjee, A. Scaling laws of resistive magnetohydrodynamic reconnection in the high-Lundquist-number, plasmoid-unstable regime. *Phys. Plasmas*, 17, 062104 (2010).

[44] Daughton, W. Role of electron physics in the development of turbulent magnetic reconnection in collisionless plasmas. *Nat. Phys.*, 7, 539–542 (2011).

[45] Nishida, K., Nishizuka, N. & Shibata, K. The role of a flux rope ejection in a three-dimensional magnetohydrodynamic simulation of a solar flare. *Astrophys. J.*, 775, L39 (2013).

[46] Mikic, Z. & Linker, J. A. Disruption of coronal magnetic field arcades. *Astrophys. J.*, 430, 898–912 (1994).

[47] Choe, G. S. & Lee, L. C. Evolution of Solar Magnetic Arcades. I. Ideal MHD Evolution under Footpoint Shearing. *Astrophys. J.*, 472, 360–371 (1996).

[48] Amari, T., Luciani, J. F., Aly, J. J., Mikic, Z. & Linker, J. Coronal Mass Ejection: Initiation, Magnetic Helicity, and Flux Ropes. I. Boundary Motion-driven Evolution. *Astrophys. J.*, 585, 1073–1086 (2003).

[49] Karpen, J. T., Antiochos, S. K. & DeVore, C. R. The mechanisms for the onset and explosive eruption of coronal mass ejections and eruptive flares. *Astrophys. J.*, 760, 81 (2012).

[50] Yardley, S. L., Green, L. M., van Driel-Gesztelyi, L., Williams, D. R. & Mackay, D. H. The role of flux cancellation in eruptions from bipolarARs. *Astrophys. J.*, 866, 8 (2018).

[51] van Ballegooijen, A. A. & Martens, P. C. H. Formation and eruption of solar prominences. *Astrophys. J.*, 343, 971–984 (1989).

[52] Jiang, C. W., Feng, X. S., Zhang, J. & Zhong, D. K. AMR simulations of magnetohydrodynamic problems by the CESE method in curvilinear coordinates. *Sol. Phys.*, 267, 463–491 (2010).

[53] Feng, X. S., et al. Three-dimensional solar wind modeling from the sun to earth by a sip-cese mhd model with a six-component grid. *Astrophys. J.*, 723, 300–319 (2010).

[54] Jiang, C. W., Wu, S. T., Feng, X. S. & Hu, Q. Data-driven MHD simulation of a flux-emerging active region leading to solar eruption. *Nat. Commun.*, 7, 11522 (2016).

[55] Brown, D. S., et al. Observations of Rotating Sunspots from TRACE. *Sol. Phys.*, 216, 79–108 (2003).

[56] Yan, X. L. & Qu, Z. Q. Rapid rotation of a sunspot associated with flares. *Astron. & Astrophys.*, 468, 1083–1088 (2007).

[57] Yan, X. L., Qu, Z. Q., Kong, D. F. & Xu, C. L. Sunspot Rotation, Sigmoidal Filament, Flare, and Coronal Mass Ejection: The Event on 2000 February 10. *Astrophys. J.*, 754, 16 (2012).

[58] Amari, T., Luciani, J. F., Aly, J. J. & Tagger, M. Very Fast Opening of a Three-dimensional Twisted Magnetic Flux Tube. *Astrophys. J. Lett.*, 466, L39–L42 (1996).

[59] Tokman, M. & Bellan, P. M. Three-dimensional Model of the Structure and Evolution of Coronal Mass Ejections. *Astrophys. J.*, 567, 1202–1210 (2002).

[60] Török, T. & Kliem, B. The evolution of twisting coronal magnetic flux tubes. *Astron. & Astrophys.*, 406, 1043–1059 (2003).

[61] DeVore, C. R. & Antiochos, S. K. Homologous Confined Filament Eruptions via Magnetic Breakout. *Astrophys. J.*, 680, 740–756 (2008).

[62] Shibata, K. & Tanuma, S. Plasmoid-induced-reconnection and fractal reconnection. *Earth, Planets and Space*, 53, 473–482 (2001).

[63] Priest, E. R. *Solar magneto-hydrodynamics.* Springer Netherlands (1987).

[64] Shiota, D., Kusano, K., Miyoshi, T., Nishikawa, N. & Shibata, K. A quantitative MHD study of the relation among arcade shearing, flux rope formation, and eruption due to the tearing instability. *J. Geophys. Res.: Space Physics*, 113, A03S05 (2008).

[65] Jiang, C., et al. How did a major confined flare occur in super solar active region 12192? *Astrophys. J.*, 828, 62 (2016).

[66] Spitzer, L. *Physics of fully ionized gas (2nd edition).* Interscience, New York (1962).

[67] Yokoyama, T. & Shibata, K. What is the condition for fast magnetic reconnection? *Astrophys. J.*, 436, L197–L200 (1994).

[68] Lazarian, A. & Vishniac, E. T. Reconnection in a weakly stochastic field. *Astrophys. J.*, 517, 700–718 (1999).

[69] Kowal, G., Lazarian, A., Vishniac, E. T. & Otmianowska-Mazur, K. Numerical tests of fast reconnection in weakly stochastic magnetic fields. *Astrophys. J.*, 700, 63–85 (2009).

[70] Aulanier, G., Janvier, M. & Schmieder, B. The standard flare model in three dimensions. I. Strong-to-weak shear transition in post-flare loops. *Astron. & Astrophys.*, 543, A110 (2012).

[71] Janvier, M., Aulanier, G., Pariat, E. & Démoulin, P. The standard flare model in three dimensions: III. Slip-running reconnection properties. *Astron. & Astrophys.*, 555, A77 (2013).

[72] Inoue, S., Hayashi, K., Shiota, D., Magara, T. & Choe, G. S. Magnetic Structure Producing X- and M-class Solar Flares in Solar Active Region 11158. *Astrophys. J.*, 770, 79 (2013).

[73] Savcheva, A., et al. The Relation between Solar Eruption Topologies and Observed Flare Features. II. Dynamical Evolution. *Astrophys. J.*, 817, 43 (2016).

[74] Liu, R., et al. Structure, stability, and evolution of magnetic flux ropes from the perspective of magnetic twist. *Astrophys. J.*, 818, 148 (2016).

[75] Duan, A., et al. A Study of Pre-flare Solar Coronal Magnetic Fields: Magnetic Flux Ropes. *Astrophys. J.*, 884, 73 (2019).

[76] Titov, V. S., Hornig, G., & Démoulin, P. Theory of magnetic connectivity in the solar corona. *J. Geophys. Res.*, 107, 1164, 2002.

[77] Berger, M. A. & Prior, C. The writhe of open and closed curves. *Journal of Physics A Mathematical General*, 39, 8321–8348 (2006).

[78] Qiu, J., Lee, J., Gary, D. E. & Wang, H. M. Motion of Flare Footpoint Emission and Inferred Electric Field in Reconnecting Current Sheets. *Astrophys. J.*, 565, 1335–1347 (2002).

[79] Jiang, C., et al. Magnetohydrodynamic simulation of the X9.3 flare on 2017 September 6: Evolving magnetic topology. *Astrophys. J.*, 869, 13 (2018).

[80] Qiu, J., Longcope, D. W., Cassak, P. A. & Priest, E. R. Elongation of Flare Ribbons. *Astrophys. J.*, 838, 17 (2017).

[81] Su, Y., Golub, L. & Van Ballegooijen, A. A. A statistical study of shear motion of the footpoints in two-ribbon flares. *Astrophys. J.*, 655, 606–614 (2007).

[82] Démoulin, P., Priest, E. R. & Lonie, D. P. Three-dimensional magnetic reconnection without null points: 2. Application to twisted flux tubes. *J. Geophys. Res.*, 101, 7631–7646 (1996).

[83] Savcheva, A., Pariat, E., van Ballegooijen, A., Aulanier, G. & DeLuca. E. Sigmoidal Active Region on the Sun: Comparison of a Magnetohydrodynamical Simulation and a Nonlinear Force-free Field Model. *Astrophys. J.*, 750, 15 (2012).

[84] Janvier, M. Electric currents in flare ribbons: Observations and three-dimensional standard model. *Astrophys. J.*, 788, 60 (2014).

[85] Jing, J., et al. Unprecedented Fine Structure of a Solar Flare Revealed by the 1.6 m New Solar Telescope. *Scientific Reports*, 6, 24319 (2016).

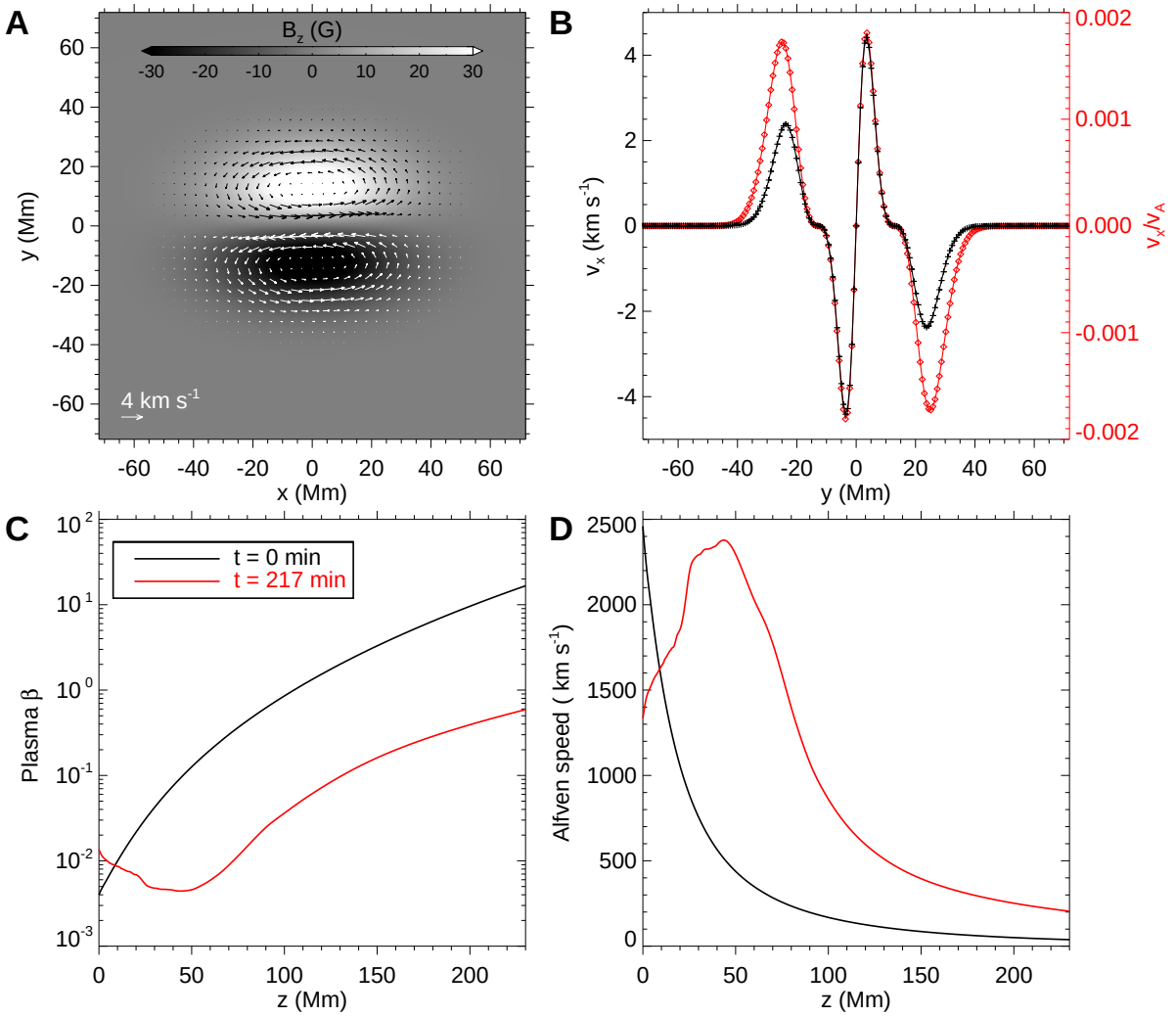

Extended Data Fig.1. Some key parameters for the settings of the simulation. (**A**) Magnetic flux distribution and surface rotation flow at the bottom surface (i.e., $z = 0$). The background is color-coded by the vertical magnetic component B_z , and the vectors show the rotation flow. (**B**) Profile of velocity (the black line) and its ratio to local Alfvén speed (the red line) along $(x, z) = 0$ line. (**C**) Plasma β (i.e., ratio of gas pressure to the magnetic pressure) profile along the central vertical line, i.e., $(x, y) = 0$. (**D**) Profile of Alfvén speed along the central vertical line. In (C) and (D), the black lines are shown for the initial values, while the red lines represent the values at time immediately prior to the eruption onset.

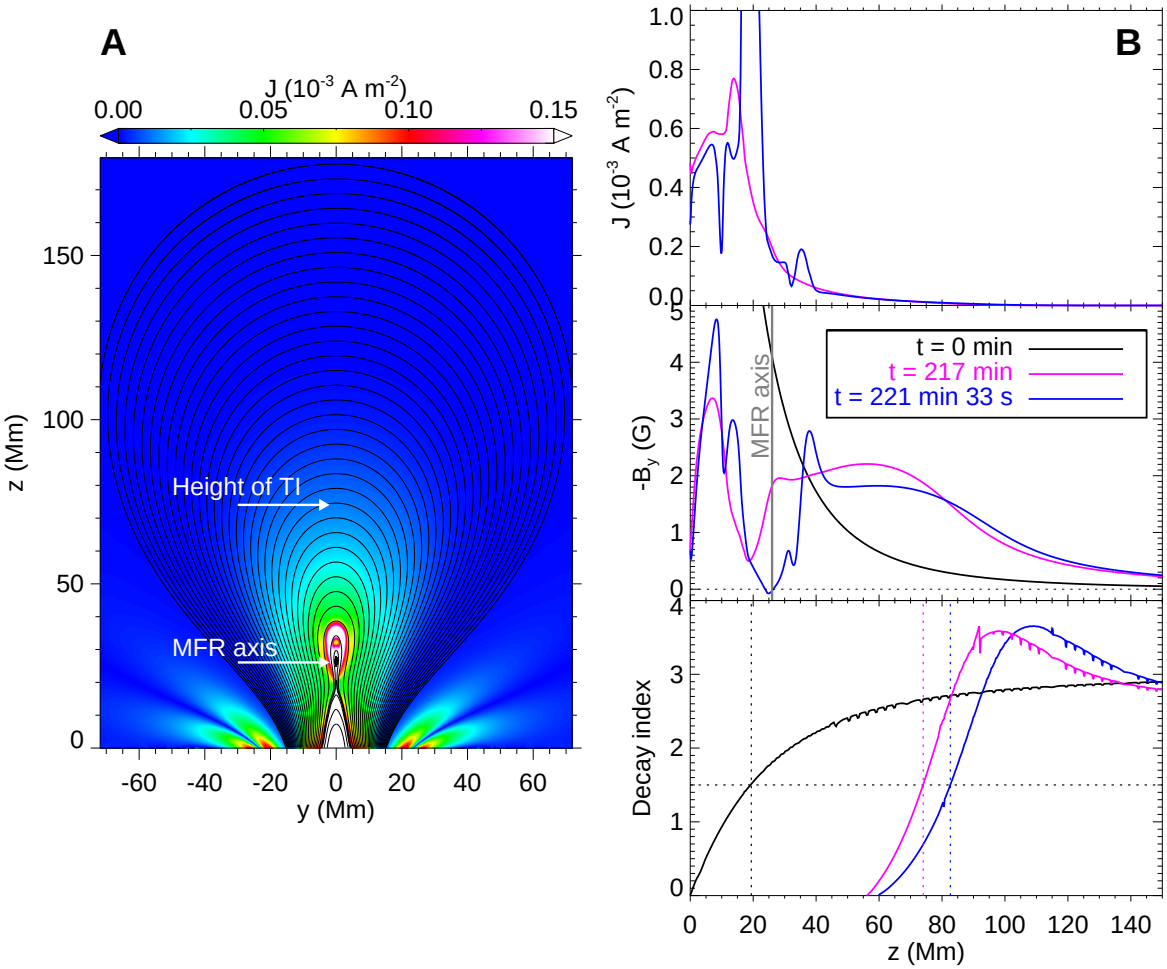

Extended Data Fig.2. Magnetic field, current density and decay index around the eruption onset. (**A**) Current density on the slice of $x = 0$ at the time when the MFR first forms during the eruption (i.e., $t = 221$ min 33 s). The black curves are projection of magnetic field lines on the slice. The lower arrow denotes the axis of the MFR. The upper arrow denotes the critical height of torus instability (TI). (**B**) From top to bottom are shown for current density, magnetic field component B_y, and decay index of B_y, respectively, along z axis (i.e., the line with both x and $y = 0$). The black, magenta, and blue curves represent results for the initial potential field ($t = 0$), the field immediately prior to the eruption onset ($t = 217$ min), and the field at $t = 221$ min 33 s, respectively. In the middle panel, the thick vertical line colored in gray denotes the height at which the MFR is initially formed. In the bottom panel, the dashed horizontal line denote the critical value (1.5) of decay index, and the dashed vertical lines denote the corresponding heights.

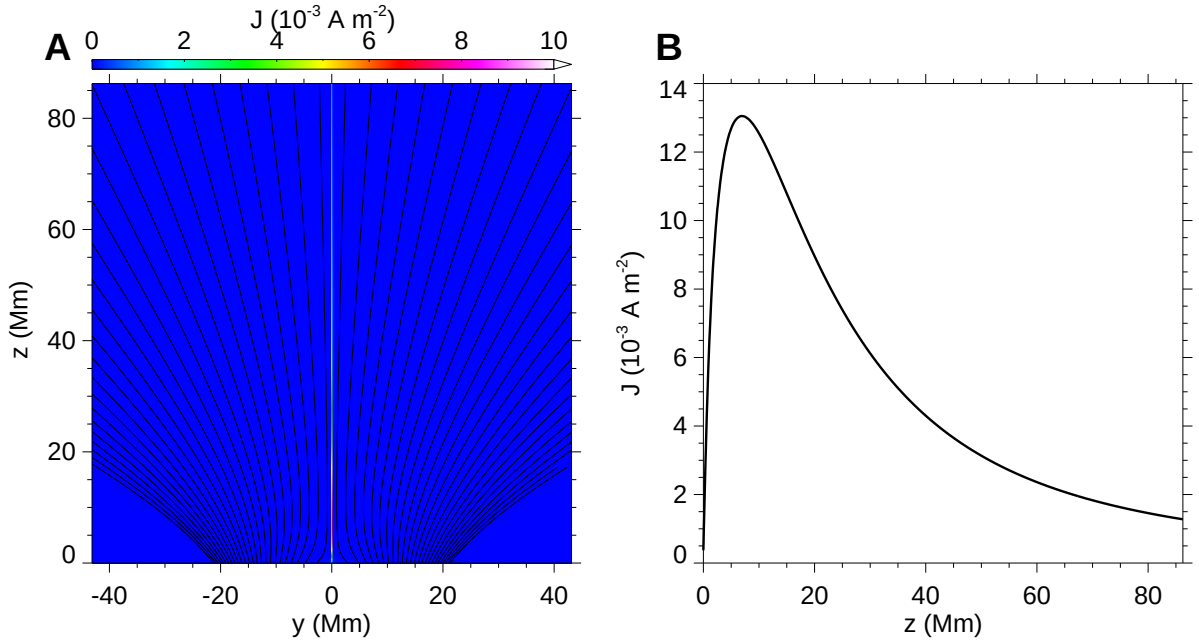

Extended Data Fig.3. The fully opened magnetic field discretized on grid with resolution of 90 **km**. **(A)** Current density distribution on the central cross section, i.e., the $x = 0$ slice, showing that current only distributes in the central line, or more exactly a CS with a finite thickness of 90 km, while all other regions are current-free. The black curves represent the magnetic field lines, which are fully opened, i.e., extending from the bottom surface to infinity. **(B)** Profile of current density along z axis.

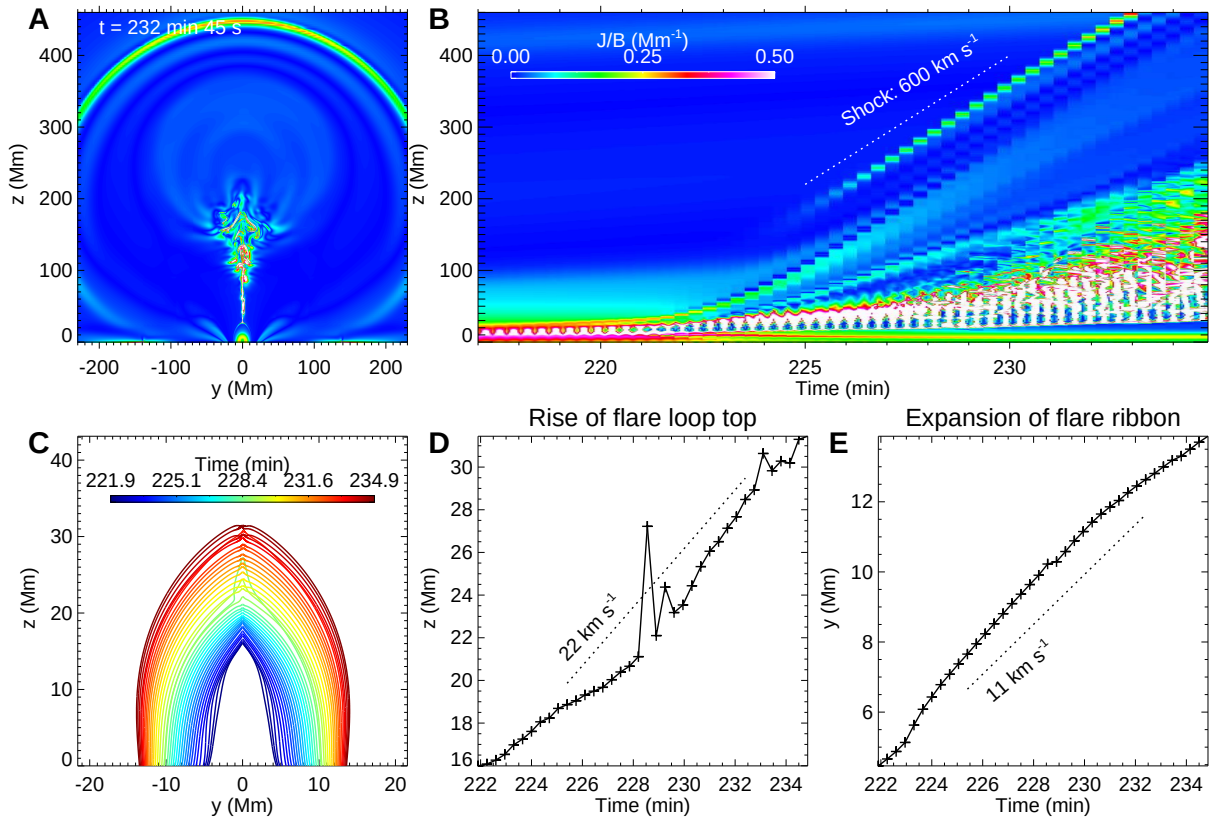

Extended Data Fig.4. Parameters that are comparable with observations. **(A)** Current distribution on the central cross section. **(B)** A time stack map of the current distribution around $x, y = 0$, which can reveal the evolution speed of the CME. **(C)** Temporal evolution of the edge of the post-flare loops. **(D)** Rising of the post-flare loop top. **(E)** Horizontal motion of the post-flare loop footpoints, which corresponds to the separation of flare ribbons. The dashed lines in **D** and **E** denote the average speeds of the motions.

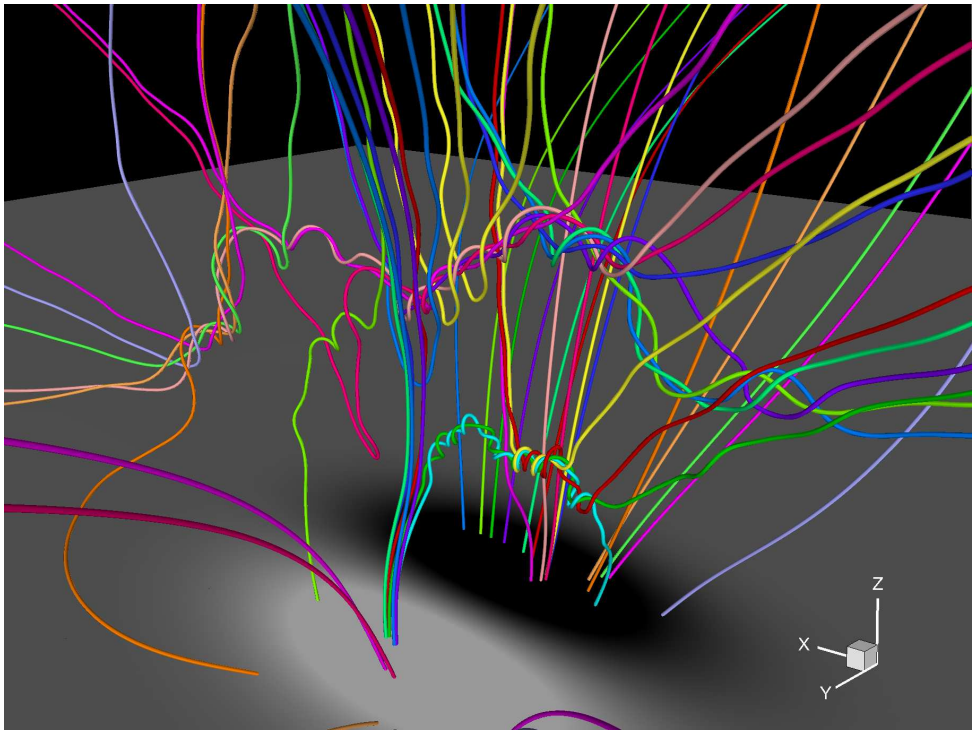

Extended Data Fig.5. Mini flux ropes formed in the reconnecting CS. The field lines are colored differently and the bottom surface is shown with the magnetic flux distribution.